



THE RADIAL VELOCITY EXPERIMENT (RAVE): FIFTH DATA RELEASE

ANDREA KUNDER¹, GEORGES KORDOPATIS¹, MATTHIAS STEINMETZ¹, TOMAŽ ZWITTER², PAUL J. McMILLAN³,
 LUCA CASAGRANDE⁴, HARRY ENKE¹, JENNIFER WOJNO¹, MARICA VALENTINI¹, CRISTINA CHIAPPINI¹, GAL MATIJEVIĆ¹,
 ALESSANDRO SIVIERO⁵, PATRICK DE LAVERNY⁶, ALEJANDRA RECIO-BLANCO⁶, ALBERT BIJAOUÏ⁶, ROSEMARY F. G. WYSE⁷,
 JAMES BINNEY⁸, E. K. GREBEL⁹, AMINA HELMI¹⁰, PAULA JOFRE^{11,12}, TERESA ANTOJA¹⁰, GERARD GILMORE¹²,
 ARNAUD SIEBERT¹³, BENOIT FAMAËY¹³, OLIVIER BIENAYMÉ¹³, BRAD K. GIBSON¹⁴, KENNETH C. FREEMAN¹⁵,
 JULIO F. NAVARRO^{16,31}, ULISSE MUNARI⁵, GEORGE SEABROKE¹⁷, BORJA ANGUIANO^{18,19}, MARUŠA ŽERJAL²,
 IVAN MINCHEV¹, WARREN REID^{19,20}, JOSS BLAND-HAWTHORN²¹, JANEZ KOS²¹, SANJIB SHARMA²¹, FRED WATSON²²,
 QUENTIN A. PARKER^{23,24}, RALF-DIETER SCHOLZ¹, DONNA BURTON¹⁸, PAUL CASS¹⁸, MALCOLM HARTLEY¹⁸, KRISTIN FIEGERT¹⁸,
 MILORAD STUPAR^{18,19}, ANDREAS RITTER²⁵, KEITH HAWKINS^{11,26}, ORTWIN GERHARD²⁷, W. J. CHAPLIN^{28,29},
 G. R. DAVIES^{28,29}, Y. P. ELSWORTH^{28,29}, M. N. LUND^{27,29}, A. MIGLIO^{27,29}, AND B. MOSSER³⁰

¹ Leibniz-Institut für Astrophysik Potsdam (AIP), An der Sternwarte 16, D-14482 Potsdam, Germany; akunder@aip.de

² Faculty of Mathematics and Physics, University of Ljubljana, Jadranska 19, 1000 Ljubljana, Slovenia

³ Lund Observatory, Lund University, Department of Astronomy and Theoretical Physics, Box 43, SE-22100, Lund, Sweden

⁴ Research School of Astronomy & Astrophysics, Mount Stromlo Observatory, The Australian National University, ACT 2611, Australia

⁵ Dipartimento di Fisica e Astronomia Galileo Galilei, Università di Padova, Vicolo dell'Osservatorio 3, I-35122 Padova, Italy

⁶ Laboratoire Lagrange, Université Côte d'Azur, Observatoire de la Côte d'Azur, CNRS, Bd de l'Observatoire, CS 34229, F-06304 Nice cedex 4, France

⁷ Department of Physics and Astronomy, Johns Hopkins University, 3400 N. Charles St, Baltimore, MD 21218, USA

⁸ Rudolf Peierls Centre for Theoretical Physics, Keble Road, Oxford OX1 3NP, UK

⁹ Astronomisches Rechen-Institut, Zentrum für Astronomie der Universität Heidelberg, Mönchhofstr. 12–14, D-69120 Heidelberg, Germany

¹⁰ Kapteyn Astronomical Institute, University of Groningen, P.O. Box 800, 9700 AV Groningen, The Netherlands

¹¹ Institute of Astronomy, University of Cambridge, Madingley Road, Cambridge CB3 0HA, UK

¹² Núcleo de Astronomía, Facultad de Ingeniería, Universidad Diego Portales, Av. Ejército 441, Santiago, Chile

¹³ Observatoire astronomique de Strasbourg, Université de Strasbourg, CNRS, UMR 7550, 11 rue de l'Université, F-67000 Strasbourg, France

¹⁴ E.A. Milne Centre for Astrophysics, University of Hull, Hull HU6 7RX, UK

¹⁵ Research School of Astronomy & Astrophysics, Australian National University, Cotter Rd., Weston, ACT 2611, Australia

¹⁶ Department of Physics and Astronomy, University of Victoria, Victoria, BC, V8P 5C2 Canada

¹⁷ Mullard Space Science Laboratory, University College London, Holmbury St Mary, Dorking RH5 6NT, UK

¹⁸ Australian Astronomical Observatory, P.O. Box 915, North Ryde, NSW 1670, Australia

¹⁹ Department of Physics and Astronomy, Macquarie University, Sydney, NSW 2109, Australia

²⁰ University of Western Sydney, Penrith South DC, NSW 1797, Australia

²¹ Sydney Institute for Astronomy, School of Physics, A28, The University of Sydney, NSW 2006, Australia

²² Anglo-Australian Observatory, P.O. Box 296, Epping, NSW 1710, Australia

²³ Department of Physics, CYM Building, The University of Hong Kong, Hong Kong, China

²⁴ The Laboratory for Space Research, The University of Hong Kong, Hong Kong, China

²⁵ Department of Astrophysical Sciences, Princeton University, 4 Ivy Ln, Princeton, NJ 08544, USA

²⁶ Department of Astronomy, Columbia University, 550 W. 120 st., New York, NY, USA

²⁷ Max-Planck-Institut fuer Ex. Physik, Giessenbachstrasse, D-85748 Garching b. Muenchen, Germany

²⁸ School of Physics and Astronomy, University of Birmingham, Edgbaston, Birmingham B15 2TT, UK

²⁹ Stellar Astrophysics Centre, Department of Physics and Astronomy, Aarhus University, DK-8000 Aarhus C, Denmark

³⁰ Observatoire de Paris, PSL Research University, CNRS, Université Pierre et Marie Curie, Université Paris Diderot, F-92195, Meudon, France

Received 2016 September 11; revised 2016 November 14; accepted 2016 November 15; published 2017 January 17

ABSTRACT

Data Release 5 (DR5) of the Radial Velocity Experiment (RAVE) is the fifth data release from a magnitude-limited ($9 < I < 12$) survey of stars randomly selected in the Southern Hemisphere. The RAVE medium-resolution spectra ($R \sim 7500$) covering the Ca-triplet region (8410–8795 Å) span the complete time frame from the start of RAVE observations in 2003 to their completion in 2013. Radial velocities from 520,781 spectra of 457,588 unique stars are presented, of which 255,922 stellar observations have parallaxes and proper motions from the Tycho-*Gaia* astrometric solution in *Gaia* DR1. For our main DR5 catalog, stellar parameters (effective temperature, surface gravity, and overall metallicity) are computed using the RAVE DR4 stellar pipeline, but calibrated using recent *K2* Campaign 1 seismic gravities and *Gaia* benchmark stars, as well as results obtained from high-resolution studies. Also included are temperatures from the Infrared Flux Method, and we provide a catalog of red giant stars in the dereddened color ($J - K_s$)₀ interval (0.50, 0.85) for which the gravities were calibrated based only on seismology. Further data products for subsamples of the RAVE stars include individual abundances for Mg, Al, Si, Ca, Ti, Fe, and Ni, and distances found using isochrones. Each RAVE spectrum is complemented by an error spectrum, which has been used to determine uncertainties on the parameters. The data can be accessed via the RAVE Web site or the VizieR database.

Key words: catalogs – Galaxy: abundances – Galaxy: kinematics and dynamics – Galaxy: stellar content – stars: abundances – surveys

³¹ CfAR Senior Fellow.

1. INTRODUCTION

The kinematics and spatial distributions of Milky Way stars help define the Galaxy we live in, and allow us to trace parts of the formation of the Milky Way. In this regard, large spectroscopic surveys that provide measurements of fundamental structural and dynamical parameters for a statistical sample of Galactic stars have been extremely successful in advancing the understanding of our Galaxy. Recent and ongoing spectroscopic surveys of the Milky Way include the RAdial Velocity Experiment (RAVE, Steinmetz et al. 2006), the Sloan Extension for Galactic Understanding and Exploration (Yanny et al. 2009), the APO Galactic Evolution Experiment (APOGEE, Eisenstein et al. 2011), the LAMOST Experiment for Galactic Understanding and Exploration (LAMOST, Zhao et al. 2012), the *Gaia*-ESO Survey (Gilmore et al. 2012), and the GALactic Archaeology with HERMES (GALAH, De Silva et al. 2015). These surveys were made possible by the emergence of wide-field multi-object spectroscopy fiber systems, technology that especially took off in the 1990s. Each survey has its own unique aspect, and together they form complementary samples in terms of capabilities and sky coverage.

Of the above mentioned surveys, RAVE was the first, designed to provide stellar parameters to complement missions that focus on astrometric information. The four previous data releases—DR1 (Steinmetz et al. 2006), DR2 (Zwitter et al. 2008), DR3 (Siebert et al. 2011), and DR4 (Kordopatis et al. 2013a)—have been the foundation for a number of studies that have advanced our understanding of especially the disk of the Milky Way (see review by Kordopatis 2014). For example, in recent years a wave-like pattern in the stellar velocity distribution was uncovered (Williams et al. 2013) and the total mass of the Milky Way was measured using the RAVE extreme-velocity stars (Piffl et al. 2014b), as was the local dark matter density (Bienaymé et al. 2014; Piffl et al. 2014a). Moreover, chemo-kinematic signatures of the dynamical effect of mergers on the Galactic disk (Minchev et al. 2014), and signatures of radial migration were detected (Kordopatis et al. 2013b; Wojno et al. 2016a). Stars tidally stripped from globular clusters were also identified (Kunder et al. 2014; Anguiano et al. 2015, 2016). RAVE further allowed for the creation of pseudo-3D maps of the diffuse interstellar band at 8620 Å (Kos et al. 2014) and for high-velocity stars to be studied (Hawkins et al. 2015).

RAVE Data Release 5 (DR5) includes not only the final RAVE observations taken in 2013, but also earlier discarded observations recovered from previous years, resulting in an additional $\sim 30,000$ RAVE spectra. This is the first RAVE data release in which an error spectrum was generated for each RAVE observation, so we can provide realistic uncertainties and probability distribution functions for the derived radial velocities and stellar parameters. We have performed a recalibration of stellar metallicities, especially improving stars of supersolar metallicity. Using the *Gaia* benchmark stars (Jofré et al. 2014; Heiter et al. 2015) as well as 72 RAVE stars with *Kepler-2* asteroseismic $\log g$ parameters (Valentini et al. 2017, hereafter V17), the RAVE $\log g$ values have been recalibrated, resulting in more accurate gravities especially for the giant stars in RAVE. The distance pipeline (Binney et al. 2014) has been improved and extended to process more accurately stars with low metallicities ($[M/H] < -0.9$ dex). Finally, by combining optical photometry from APASS (Munari et al. 2014) with 2MASS (Skrutskie et al. 2006) we

have derived temperatures from the infrared flux method (IRFM; Casagrande et al. 2010).

Possibly the most distinct feature of DR5 is the extent to which it complements the first significant data release from *Gaia*. The successful completion of the *Hipparcos* mission and publication of the catalog (ESA 1997) demonstrated that space astrometry is a powerful technique to measure accurate distances to astronomical objects. Already in RAVE-DR1 (Steinmetz et al. 2006), we looked forward to the results from the ESA cornerstone mission *Gaia*, because this space-based mission’s astrometry of Milky Way stars will have ~ 100 times better astrometric accuracies than its predecessor, *Hipparcos*. Although *Gaia* has been launched and data collection is ongoing, a long enough time baseline has to have elapsed for sufficient accuracy of a global reduction of observations (e.g., five years for *Gaia* to yield positions, parallaxes, and annual proper motions at an accuracy level of 5–25 μas , Michalik et al. 2014). To expedite the use of the first *Gaia* astrometry results, the approximate positions at the earlier epoch (around 1991) provided by the Tycho-2 Catalogue (Høg et al. 2000) can be used to disentangle the ambiguity between parallax and proper motion in a shorter stretch of *Gaia* observations. These Tycho-*Gaia* astrometric solution (TGAS) stars therefore have positions, parallaxes, and proper motions before the global astrometry from *Gaia* can be released. There are 215,590 unique RAVE stars in TGAS, so for these stars we now have space-based parallaxes and proper motions from *Gaia* DR1 in addition to stellar parameters, radial velocities, and in many cases chemical abundances. The Tycho-2 stars observed by RAVE in a homogeneous and well-defined manner can be combined with the released TGAS stars to exploit the larger volume of stars for which astrometry with milliarcsecond accuracy exists, for an extraordinary return in scientific results. We note that in a companion paper, a data-driven reanalysis of the RAVE spectra using *The Cannon* model has been carried out (Casey et al. 2016, hereafter C16), which presents the derivation of T_{eff} , surface gravity $\log g$, and $[\text{Fe}/\text{H}]$, as well as chemical abundances of giants of up to seven elements (O, Mg, Al, Si, Ca, Fe, Ni).

In Section 2, the selection function of the RAVE DR5 stars is presented—further details can be found in Wojno et al. (2016b, hereafter W16). The RAVE observations and reductions are summarized in Section 3. An explanation of how the error spectra were obtained is found in Section 4, and Section 5 summarizes the derivation of radial velocities from the spectra. In Section 6, the procedure used to extract atmospheric parameters from the spectrum is described and the external verification of the DR5 T_{eff} , $\log g$, and $[M/H]$ values is discussed in Section 7. The dedicated pipelines to extract elemental abundances and distances are described in Sections 8 and 9, respectively—DR5 gives radial velocities for all RAVE stars but elemental abundances and distances are given for subsamples of RAVE stars that have signal-to-noise ratio (S/N) > 20 and the most well-defined stellar parameters. Temperatures from the IRFM are presented in Section 10. In Section 11 we present gravities for the red giants based on asteroseismology by the method of V17. A comparison of the stellar parameters in the RAVE DR5 main catalog to other stellar parameters for RAVE stars (e.g., those from C16) is provided in Section 12. The final sections, Sections 13 and 14, provide a summary of the difference between DR4 and DR5, and an overview of DR5, respectively.

2. SURVEY SELECTION FUNCTION

Rigorous exploitation of DR5 requires knowledge of RAVE’s selection function, which was recently described by W16. Here we provide only a summary.

The stars for the RAVE input catalog were selected from their I -band magnitudes, focusing on bright stars ($9 < I < 12$) in the Southern Hemisphere, but the catalog does contain some stars that are either brighter or fainter, in part because stars were selected by extrapolating data from other sources, such as Tycho-2 and SuperCOSMOS before DENIS was available in 2006 (see Section 2 of the DR4 paper by Kordopatis et al. 2013a for details). As the survey progressed, the targets in the input catalog were grouped into four I -band magnitude bins: 9.0–10.0, 10.0–10.75, 10.75–11.5, and 11.5–12.0, which helped mitigate problems of fiber cross-talk. This led to a segmented distribution of RAVE stars in I -band magnitudes, but the distributions in other passbands are closely matched by Gaussians (see, e.g., Figure 11 in Munari et al. 2014). For example, in the B -band, the stars observed by RAVE have a nicely Gaussian distribution, peaking at $B = 12.62$ with $\sigma = 1.11$ mag.

The initial target selection was based only on the apparent I -band magnitude, but a color criterion ($J - K_s \geq 0.5$) was later imposed in regions close to the Galactic plane (Galactic latitude $|b| < 25^\circ$) to bias the survey toward giants. Therefore, the probability, S , of a star being observed by the RAVE survey is

$$S \propto S_{\text{select}}(l, b, I, J - K_s), \quad (1)$$

where l is Galactic longitude. W16 determine the function S_{select} both on a field-by-field basis, so time-dependent effects can be captured, and with Hierarchical Equal-Area iso-Latitude Pixelisation (HEALPix) (e.g., Górski et al. 2005), which divides the sky into equal-area pixels, as regularly distributed as possible. The sky is divided into 12,288 pixels ($N_{\text{side}} = 32$), which results in a pixel area of $\simeq 3.36$ deg², and we consider only the selection function evaluated with HEALPix for quality control and variability tests, because RAVE fields overlap on the sky.

The parent RAVE sample is constructed by first discarding all repeat observations, keeping only the observation with the highest S/N. Then observations that were not conducted as part of the typical observing strategy (e.g., calibration fields) were removed. Finally, all stars with $|b| < 25^\circ$ that were observed despite violating the color criterion $J - K_s \geq 0.5$ were dismissed. After applying these cuts, we are left with 448,948 stars, or 98% of all stars targeted by RAVE. These define the RAVE DR5 core sample (survey footprint). The core sample is complemented by targeted observations (e.g., open clusters), mainly for calibration and testing.

The number of RAVE stars (N_{RAVE}) in each HEALPix pixel is then counted as a function of $I_{2\text{MASS}}$. We apply the same criteria to two photometric all-sky surveys, 2MASS and Tycho-2, to discover how many stars could, in principle, have been observed. After these catalogs were purged of spurious measurements, we obtain $N_{2\text{MASS}}$ and N_{TYCHO2} and can compute the completeness of RAVE as a function of magnitude for both 2MASS and Tycho-2 as $N_{\text{RAVE}}/N_{2\text{MASS}}$ and $N_{\text{RAVE}}/N_{\text{TYCHO2}}$.

Figure 1 shows the DR5 completeness with respect to Tycho-2 as a function of magnitude. It is evident that RAVE avoids the Galactic plane, and we find that the coverage on the sky is highly anisotropic, with a significant drop-off in

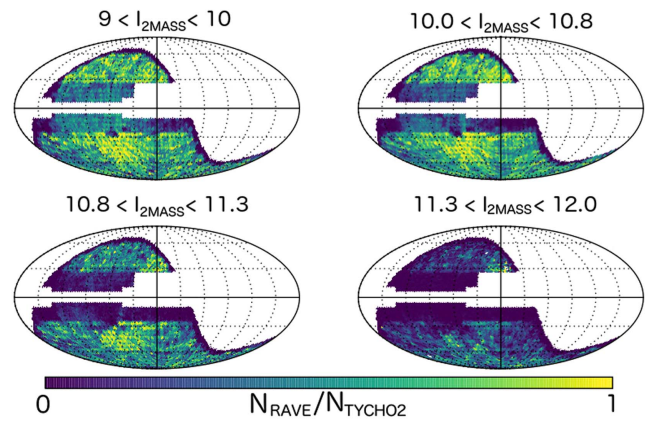


Figure 1. Mollweide projection of Galactic coordinates of the completeness of the stars in Tycho-2 for which RAVE DR5 radial velocity measurements are available for the core sample. Each panel shows the completeness over a different magnitude bin, where the HEALPix pixels are color-coded by the fractional completeness ($N_{\text{RAVE}}/N_{\text{TYCHO2}}$).

Table 1
Contents of RAVE DR5

Property	In DR5
RAVE stellar spectra	520,781
Unique stars observed	457,588
Stars with ≥ 3 visits	8000
Spectra/unique stars with S/N > 20	478,161/423,283
Spectra/unique stars with S/N > 80	66,888/60,880
Stars with $\text{AlgoConv} \neq 1^a$	428,952
Stars with elemental abundances	339,750
Stars with morphological flags n, d, g, h, o	394,612
Tycho-2 + RAVE stellar spectra/unique stars	309,596/264,276
TGAS + RAVE stellar spectra/unique stars	255,922/215,590

Note.

^a For a discussion of AlgoConv see Section 6.1.

completeness at the fainter magnitudes. A similar result is seen for $N_{\text{RAVE}}/N_{2\text{MASS}}$ (W16). However, in $N_{\text{RAVE}}/N_{2\text{MASS}}$, there is a significantly higher completeness at low Galactic latitudes ($|b| < 25^\circ$) for the fainter magnitude bins.

Because stars that passed the photometric cuts were randomly selected for observation, RAVE DR5 is free of kinematic bias. Hence, the contents of DR5 (see Table 1) are representative of the Milky Way for the specific magnitude interval. A number of peculiar and rare objects are included. The morphological flags of Matijević et al. (2012) allow one to identify the normal single stars (90%–95%), and those that are unusual—the peculiar stars include various types of spectroscopic binary and chromospherically active stars. The stars falling within the footprint of the RAVE selection function described in W16 are provided in https://www.rave-survey.org/project/documentation/dr5/rave_completeness_pbp/.

3. SPECTRA AND THEIR REDUCTION

The RAVE spectra were taken using the multi-object spectrograph 6dF (6 degree field) on the 1.2 m UK Schmidt Telescope of the Australian Astronomical Observatory (AAO). A total of 150 fibers could be allocated in one pointing, and the covered spectral region (8410–8795 Å) at an effective resolution of $R = \lambda/\Delta\lambda \sim 7500$ was chosen as analogous to the

wavelength range of *Gaia*'s Radial Velocity Spectrometer (see Sections 2 and 3 of the DR1 paper by Steinmetz et al. 2006 for details).

The RAVE reductions are described in detail in DR1 Section 4 and upgrades to the process are outlined in DR3 Section 2. In DR5 further improvements have been made to the Spectral Parameters And Radial Velocity (SPARV) pipeline, the DR3 pipeline that carries out the continuum normalization, masks bad pixels, and provides RAVE radial velocities. The most significant is that instead of the reductions being carried out on a field-by-field basis, single fiber processing was implemented. Therefore, if there were spectra within a RAVE field that simply could not be processed, instead of the whole field failing and being omitted from the final RAVE catalog, only the problematic spectra are removed. This is one reason why DR5 has more stars than the previous RAVE data releases.

The DR5 reduction pipeline is able to process the problematic DR1 spectra, and it produces error spectra. An overhaul of bookkeeping and process control led to identification of multiple copies of the same observation and of spectra with corrupted FITS headers. Some RAVE IDs have changed from DR4, and some stars released in DR4 could not be processed by the DR5 pipeline. The vast majority of these stars have low signal-to-noise ratios ($S/N < 10$). Details are provided in Appendix A; less than 0.1% of RAVE spectra were affected by bookkeeping inconsistencies.

4. ERROR SPECTRA

The wavelength range of the RAVE spectra is dominated by strong spectral lines: for a majority of stars, the dominant absorption features are due to the infrared calcium triplet (CaT), which in hot stars gives way to the Paschen series of hydrogen. Also present are weaker metallic lines for the solar-type stars and molecular bands for the coolest stars. Within an absorption trough the flux is small, so shot noise is more significant in the middle of a line than in the adjacent continuum. Error levels increase also at wavelengths of airglow sky emission lines, which have to be subtracted during reductions. As a consequence, a single number, usually reported as S/N , is not an adequate quantification of the observational errors associated with a given spectrum.

For this reason, DR5 provides error spectra that comprise uncertainties ("errors") for each pixel of the spectrum. RAVE spectra generally have a high S/N in the continuum (its median value is $S/N \sim 40$), and there shot noise dominates the errors. Denoting the number of counts accumulated in the spectrum before sky subtraction by N_u , the corresponding number after sky subtraction by N_s , and the effective gain by g , the shot noise is $N = \sqrt{gN_u}$ and the signal is $S = gN_s$. The appearance of N_u rather than N_s in the relation for N reflects the fact that noise is enhanced near night-sky emission lines. As a consequence the S/N is decreased both within profiles of strong stellar absorption lines (where N_s is small) and near sky emission lines. The gain g is determined using the count versus magnitude relation (see Equation (1) from Zwitter et al. 2008). Its value ($g = 0.416e^-/ADU$) reflects systematic effects on a pixel-to-pixel scale that lower the effective gain to this level.

Telluric absorptions are negligible in the RAVE wavelength range (Munari 1999). RAVE observations from Siding Spring generally show a sky signal with a low continuum level, even when observed close to the Moon. The main contributors to the sky spectrum are therefore airglow emission lines, which

belong to three series: OH transitions 6–2 at $\lambda < 8651 \text{ \AA}$, OH transitions 7–3 at $\lambda > 8758 \text{ \AA}$, and O_2 bands at $8610 \text{ \AA} < \lambda < 8710 \text{ \AA}$. Wavelengths of OH lines are listed in the file `linelists$skyines.dat`, which is part of the IRAF³² reduction package, while the physics of their origin is nicely summarized at <http://www.iafe.uba.ar/aeronomia/airglow.html>. One needs to be careful when analyzing stellar lines with superimposed airglow lines. Apart from increasing the noise levels, these lines may not be perfectly subtracted, because they can be variable on angular scales of degrees and on timescales of minutes, whereas the telescope's field of view is $6'.7$ and the exposure time was typically 50 minutes.

Evaluation of individual reduction steps (see Zwitter et al. 2008) shows that fiber cross-talk and scattered light have only a small influence on error levels. In particular, a typical level of fiber cross-talk residuals is $0.0014f$, where f is the ratio between flux of an object in an adjacent fiber and flux of the object in question. Fiber cross-talk suffers from moderate systematic effects (variable point-spread function profiles across the wavelength range), but even at the edges of the spectral range these effects do not exceed a level of 1%. Scattered light typically contributes $\sim 5\%$ of the flux level of the spectral tracing. So its effect on noise estimation is not important, and we were not able to identify any systematics. Finally, RAVE observes in the near-IR and uses a thinned CCD chip, so an accurate subtraction of interference fringes is needed. Tests show that fringe patterns for the same night and for the same focal plate typically stay constant to within 1% of the flat-field flux level. As a result scattered light and fringing only moderately increase the final noise levels. Together, scattered light and fringing are estimated to contribute a relative error of $\sim 0.8\%$, which is added in quadrature to the prevailing contribution of shot noise discussed above.

Finally we note that fluxes and therefore noise levels for individual pixels of a given spectrum are not independent of each other, but are correlated because of a limited resolving power of RAVE spectra. So the final noise spectrum was smoothed with a window with a width of 3 pixels in the wavelength direction, which corresponds to the FWHM for a resolving power of RAVE spectra.

For each pixel in a RAVE spectrum, we invoke a Gaussian with a mean and standard deviation as measured from the same pixel of the corresponding error spectrum. A new spectrum is therefore generated that can be roughly interpreted as an alternative measurement of the star (although note that the error spectrum does not take every possible measurement uncertainty into account as discussed above). We then can redetermine our radial velocity for these resampled data, and it will differ slightly from that obtained from the actual observed spectrum. Repeating this resampling process and monitoring the resulting estimates of radial velocity, we get a distribution of the radial velocity from which we can then infer an uncertainty.

The raw errors as derived in the error spectra are propagated into both the radial velocities and stellar parameters presented here. This process allows a better assessment of the uncertainties, especially of stars with low S/N or hot stars, where the CaT is not as prominent. Figure 2 shows the mean radial velocity from the resulting estimates of radial velocity of 100 resampled spectra for low S/N stars. For most RAVE

³² IRAF is distributed by the National Optical Astronomy Observatory, which is operated by the Association of Universities for Research in Astronomy (AURA) under a cooperative agreement with the National Science Foundation.

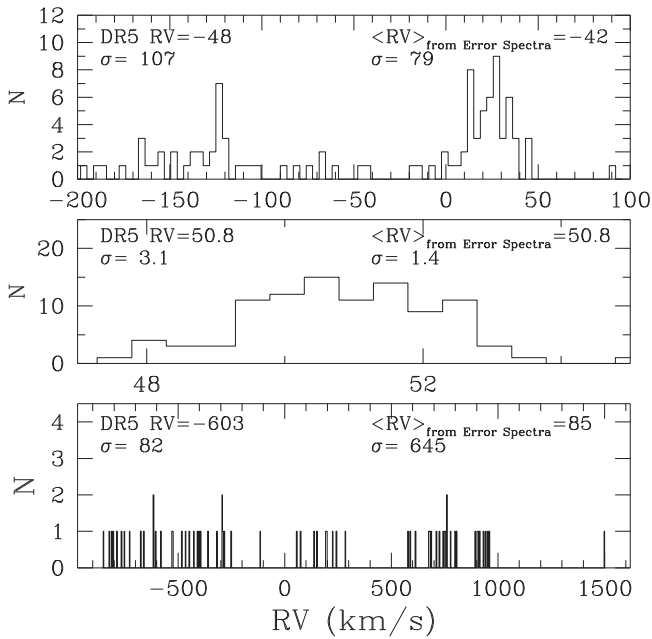


Figure 2. Derived radial velocities and dispersion from resampling the RAVE spectra 100 times using the error spectra. The top panel shows the radial velocity distribution from an $S/N = 5$ star with $T_{\text{eff}} = 3620$ K, the middle panel shows the radial velocity distribution from an $S/N = 13$ star with $T_{\text{eff}} = 5050$ K, and the bottom panel shows the radial velocity distribution from an $S/N = 8$ star with $T_{\text{eff}} = 7250$ K. The standard deviation of the radial velocity as derived from the error spectrum leads to more realistic uncertainty estimates for especially the hot stars.

stars, the errors in radial velocity are consistent with a Gaussian (see middle panel), but for the more problematic hot stars, or those with low S/N , this is clearly not the case.

Each RAVE spectrum was resampled from its error spectrum 10 times. Whereas our tests indicate that a larger number of resamplings (~ 60) would be ideal for the more problematic spectra, 10 resamplings were chosen as a compromise between computing time and the relatively small number of RAVE spectra with low S/N and hot stars that would benefit from additional resamplings. For $\sim 97.5\%$ of the RAVE sample, there is 1σ or less difference in the radial velocity and radial velocity dispersions when resampling the spectrum 10 or 100 times. In DR5, we provide both the formal error in radial velocity, which is a measure of how well the cross-correlation of the RAVE spectrum against a template spectrum was matched, and the standard deviation and median absolute deviation (MAD) in heliocentric radial velocity from a spectrum resampled 10 times.

5. RADIAL VELOCITIES

The DR5 radial velocities are derived in an identical manner to in those in DR4. The process of velocity determination is explained by Siebert et al. (2011). Templates are used to measure the radial velocities (RVs) in a two-step process. First, using a subset of 10 template spectra, a preliminary estimate of the RV is obtained, which has a typical accuracy better than 5 km s^{-1} . A new template is then constructed using the full template database described in Zwitter et al. (2008), from which the final, more precise RV is obtained. This has a typical accuracy better than 2 km s^{-1} .

The internal error in RV, $\sigma(\text{RV})$, comes from the `xcsao` task within IRAF, and therefore describes the error on the

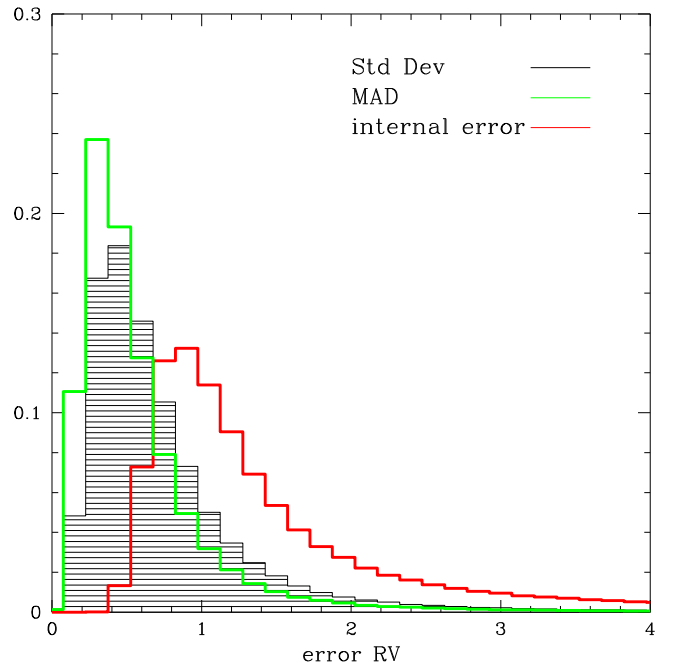


Figure 3. Histograms of the errors on the radial velocities of the DR5 stars, derived from resampling the DR5 spectra 10 times using their associated error spectra. The filled black histogram shows the standard deviation distributions and the green histogram shows the MAD estimator distribution. The red histogram shows the internal error in radial velocity obtained from cross-correlating the RAVE spectra with a template.

determination of the maximum of the correlation function. It was noticed that for some stars, particularly those with $\sigma(\text{RV}) > 10 \text{ km s}^{-1}$, $\sigma(\text{RV})$ was underestimated. The inclusion of error spectra in DR5 largely remedies this problem, and the standard deviation and MAD provide independent measures of the RV uncertainties (see Figure 2). Uncertainties derived from the error spectra are especially useful for stars that have low S/N or high temperatures. Figure 3 shows the errors from the resampled spectra compared to the internal errors. For the majority of RAVE stars, the uncertainty in RV is dominated by the cross-correlation between the RAVE spectrum and the RV template, and not by the array of uncertainties (“errors”) for each pixel of the RAVE spectrum.

Repeated RV measurements have been used to characterize the uncertainty in the RVs. There are 43,918 stars that have been observed more than once; the majority (82%) of these stars have two measurements, and six RAVE stars were observed 13 times. The histogram of the RV scatter between the repeat measurements peaks at 0.5 km s^{-1} , and has a long tail at larger scatter. This extended scatter is due both to variability from stellar binaries and to problematic measurements. If stars are selected that have radial velocities derived with high confidence, e.g., stars with $|\text{correctionRV}| < 10 \text{ km s}^{-1}$, $\sigma(\text{RV}) < 8 \text{ km s}^{-1}$, and $\text{correlationCoeff} > 10$ (see Kordopatis et al. 2013a), then the scatter of the repeat measurements peaks at 0.17 km s^{-1} and the tail is reduced by 90%.

The zero-point in RV has already been evaluated in the previous data releases. The exercise is repeated here, with the inclusion of a comparison to APOGEE and *Gaia*-ESO, and the summary of the comparisons to different samples is given in Table 2. Our comparison sample comprises the data from the Geneva–Copenhagen survey (GCS, Nordström et al. 2004) as

Table 2
External RV Samples Compared to RAVE DR5

Sample	N_{obs}	$\langle \Delta RV \rangle$	$\sigma_{\Delta RV} (\sigma_{clip}, n_{rej})$
GCS	1020	0.31	1.76 (3, 113)
Chubak	97	-0.07	1.28 (3, 2)
Ruchti	443	0.79	1.79 (3, 34)
Asiago	47	-0.22	2.98 (3, 0)
ANU 2.3 m	197	-0.58	3.13 (3, 16)
OHP Elodie	13	-0.49	2.45 (3, 2)
OHP Sophie	43	0.83	1.58 (3, 4)
APOGEE	1121	-0.11	1.87 (3, 144)
<i>Gaia</i> -Eso	106	-0.14	1.68 (3, 15)

well as high-resolution echelle follow-up observations of RAVE targets at the ANU 2.3 m telescope, the Asiago Observatory, the Apache Point Observatory (Ruchti et al. 2011), and Observatoire de Haute Provence using the instruments Elodie and Sophie. Sigma-clipping is used to remove contamination by spectroscopic binaries or problematic measurements, and the mean $\Delta(RV)$ given is $\Delta(RV) = RV_{DR5} - RV_{ref}$. As seen previously, the agreement in zero-point between RAVE and the external sources is better than 1 km s^{-1} .

6. STELLAR PARAMETERS AND ABUNDANCES

6.1. Atmospheric Parameter Determinations

RAVE DR5 stellar atmospheric parameters— T_{eff} , $\log g$, and $[M/H]$ —have been determined using the same stellar parameter pipeline as in DR4. The details can be found in Kordopatis et al. (2011) and the DR4 paper (Kordopatis et al. 2013a), but a summary is provided here.

The pipeline is based on the combination of a decision tree, DEGAS (Bijaoui et al. 2012), to renormalize the spectra iteratively and obtain stellar parameter estimations for the low S/N spectra, and a projection algorithm MATISSE (Recio-Blanco et al. 2006) to derive the parameters for stars having high S/N. The threshold above which MATISSE is preferred to DEGAS is based on tests performed with synthetic spectra (see Kordopatis et al. 2011) and has been set to $S/N = 30 \text{ pixel}^{-1}$.

The learning phase of the pipeline is carried out using synthetic spectra computed with the Turbospectrum code (Alvarez & Plez 1998) combined with MARCS model atmospheres (Gustafsson et al. 2008) assuming local thermodynamic equilibrium (LTE) and hydrostatic equilibrium. The cores of the CaT lines are masked in order to avoid issues such as non-LTE effects in the observed spectra, which could affect our parameter determination.

The stellar parameters covered by the grid are between 3000 and 8000 K for T_{eff} , 0 and 5.5 for $\log g$, and -5 to $+1$ dex in metallicity. Varying α -abundances ($[\alpha/Fe]$) as a function of metallicity are also included in the learning grid, but are not a free parameter. The line list was calibrated on the Sun and Arcturus (Kordopatis et al. 2011).

The pipeline is run on the continuum-normalized, radial velocity-corrected RAVE spectra using a soft conditional constraint based on the $2MASS J - K_s$ colors of each star. This restricted the solution space and minimized the spectral degeneracies that exist in the wavelength range of the CaT (Kordopatis et al. 2011). Once a first set of parameters is obtained for a given observation, we select pseudo-continuum windows to renormalize the input spectrum based on the

pseudo-continuum shape of the synthetic spectrum that has the parameters determined by the code, and the pipeline is run again on the modified input. This step is repeated 10 times, which is usually enough for convergence of the continuum shape to be reached and hence to obtain a final set of parameters (see, however, next paragraph).

Once the spectra have been parameterized, the pipeline provides one of the five quality flags for each spectrum:³³

1. “0”: The analysis was carried out as desired. The renormalization process converged, as did MATISSE (for high S/N spectra) or DEGAS (for low S/N spectra).
2. “1”: Although the spectrum has a sufficiently high S/N to use the projection algorithm, the MATISSE algorithm did not converge. Stellar parameters for stars with this flag are not reliable. Approximately 6% of stars are affected by this.
3. “2”: The spectrum has a sufficiently high S/N to use the projection algorithm, but MATISSE oscillates between two solutions. The reported parameters are the mean of these two solutions. In general the oscillation happens for a set of parameters that are nearby in parameter space, and computing the mean is a sensible thing to do. However, this is not always the case, for example if the spectrum contains artifacts. Then the mean may not provide accurate stellar parameters. Spectra with a flag of “2” could be used for analyses, but with caution.
4. “3”: MATISSE gives a solution that is extrapolated from the parameter range of the learning grid, and the solution is forced to be the one from DEGAS. For spectra having artifacts but high S/N overall, this is a sensible thing to do, because DEGAS is less sensitive to such discrepancies. However, for the few hot stars that have been observed by RAVE, adopting this approach is not correct. A flag of “3” and $T_{eff} > 7750 \text{ K}$ is very likely to indicate that this is a hot star with $T_{eff} > 8000 \text{ K}$ and hence that the parameters associated with that spectrum are not reliable.
5. “4”: This flag will appear only for low S/N stars. For metal-poor giants, the spectral lines available are neither strong enough nor numerous enough to have DEGAS successfully parameterize the star. Tests on synthetic spectra have shown that to derive reliable parameters the settings used to explore the branches of the decision tree need to be changed from the parameters adopted for the rest of the parameter space. A flag “4” therefore marks this change in the setting for bookkeeping purposes, and the spectra associated with this flag should be safe for any analysis.

The several tests performed for DR4 as well as the subsequent science papers have indicated that the stellar parameter pipeline is globally robust and reliable. However, being based on synthetic spectra that may not match the real stellar spectra over the entire parameter range, the direct outputs of the pipeline need to be calibrated on reference stars in order to minimize possible offsets.

6.2. Metallicity Calibrations

In DR4, the calibration of metallicity proved to be the most critical and important one. Using a set of reference stars for

³³ The flags are unchanged as compared to DR4.

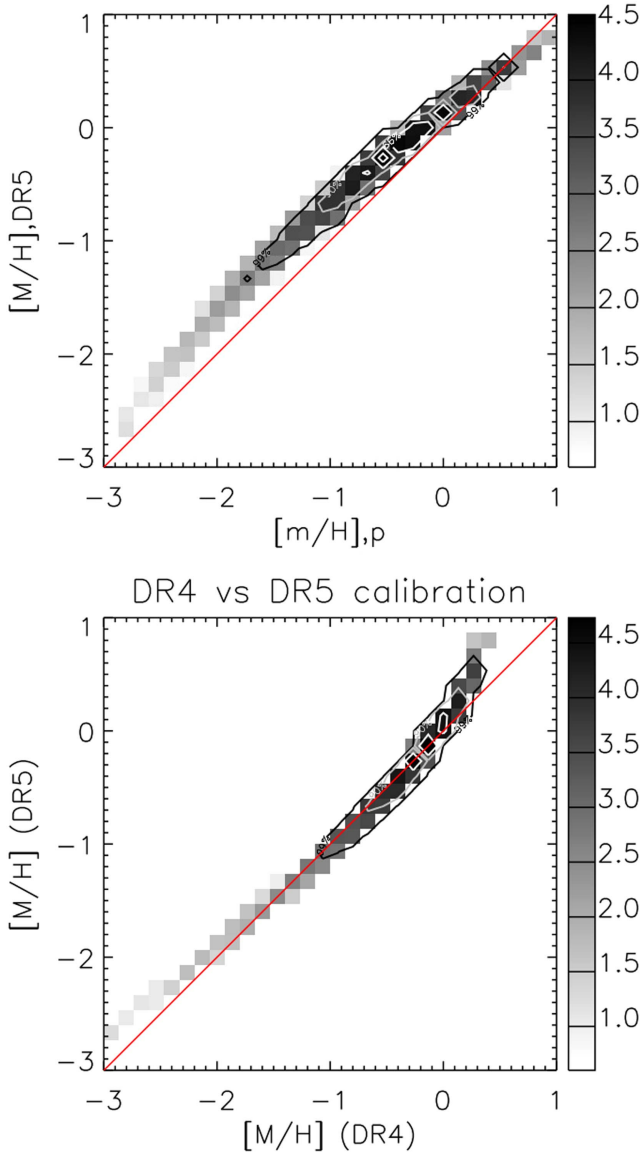


Figure 4. Top: the calibrated DR5 $[M/H]$ is compared to the uncalibrated DR5 $[M/H]_p$. Bottom: a comparison of $[M/H]$ from DR5 with $[M/H]$ from DR4. The changes occur mostly at the metal-rich end, as our reference sample now contains more high-metallicity stars. The gray scale bar indicates $\log_{10}(N)$ of stars in a bin, and the contour lines contain 33%, 66%, 90%, and 99% of the sample.

which metallicity determinations were available in the literature (usually derived from high-resolution spectra), a second-order polynomial correction, based on surface gravity and raw metallicity, was applied in DR4. This corrected the metallicity offsets with the external data sets of Pasquini et al. (2004), Pancino et al. (2010), Cayrel et al. (2004), Ruchti et al. (2011), and the PASTEL database (Soubiran et al. 2010). For DR5, we relied on the same approach. However, we added reference stars to the set used in DR4, with the focus on expanding our calibrating sample toward the high-metallicity end to better calibrate the tails of the distribution function. This calibration is based on the crossmatch of RAVE targets with the catalogs of Worley et al. (2012) and Adibekyan et al. (2013), as well as the *Gaia* benchmark stellar spectra. The metallicity of the *Gaia* benchmark stars is taken from Jofré et al. (2014), where a library of *Gaia* benchmark stellar spectra was specially

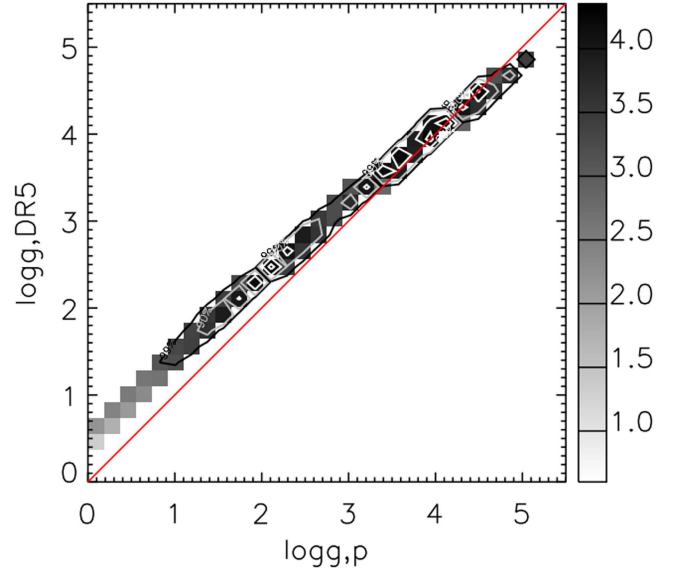


Figure 5. As Figure 4 except it compares the calibrated DR5 $\log g$ with the uncalibrated DR5 $\log g_p$. Contours as in Figure 4.

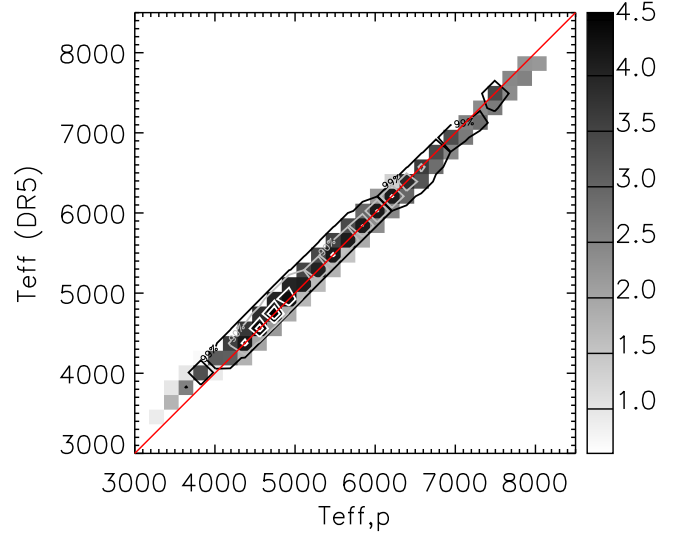


Figure 6. As Figure 4 except it compares the calibrated DR5 T_{eff} with the uncalibrated DR5 $T_{\text{eff},p}$. Contours as in Figure 4.

prepared to match RAVE data in terms of wavelength coverage, resolution, and spectral spacing. This was done following the procedure described in Blanco-Cuaresma et al. (2014). Our calibration has already been successfully used in Kordopatis et al. (2015), Wojno et al. (2016a), and Antoja et al. (2015). The calibration relation for DR5 is

$$\begin{aligned}
 [M/H] = & [M/H]_p - (-0.276 + 0.044 \log g_p \\
 & - 0.002 \log g_p^2 + 0.248 [M/H]_p \\
 & - 0.007 [M/H]_p \log g_p + 0.078 [M/H]_p^2), \quad (2)
 \end{aligned}$$

where $[M/H]$ is the calibrated metallicity, and $[M/H]_p$ and $\log g_p$ are, respectively, the uncalibrated (raw output from the pipeline) metallicity and surface gravity. The effect of the calibration on the raw output can be seen in the top panel of Figure 4. The bottom panel shows that in the range $(-2, 0)$ the

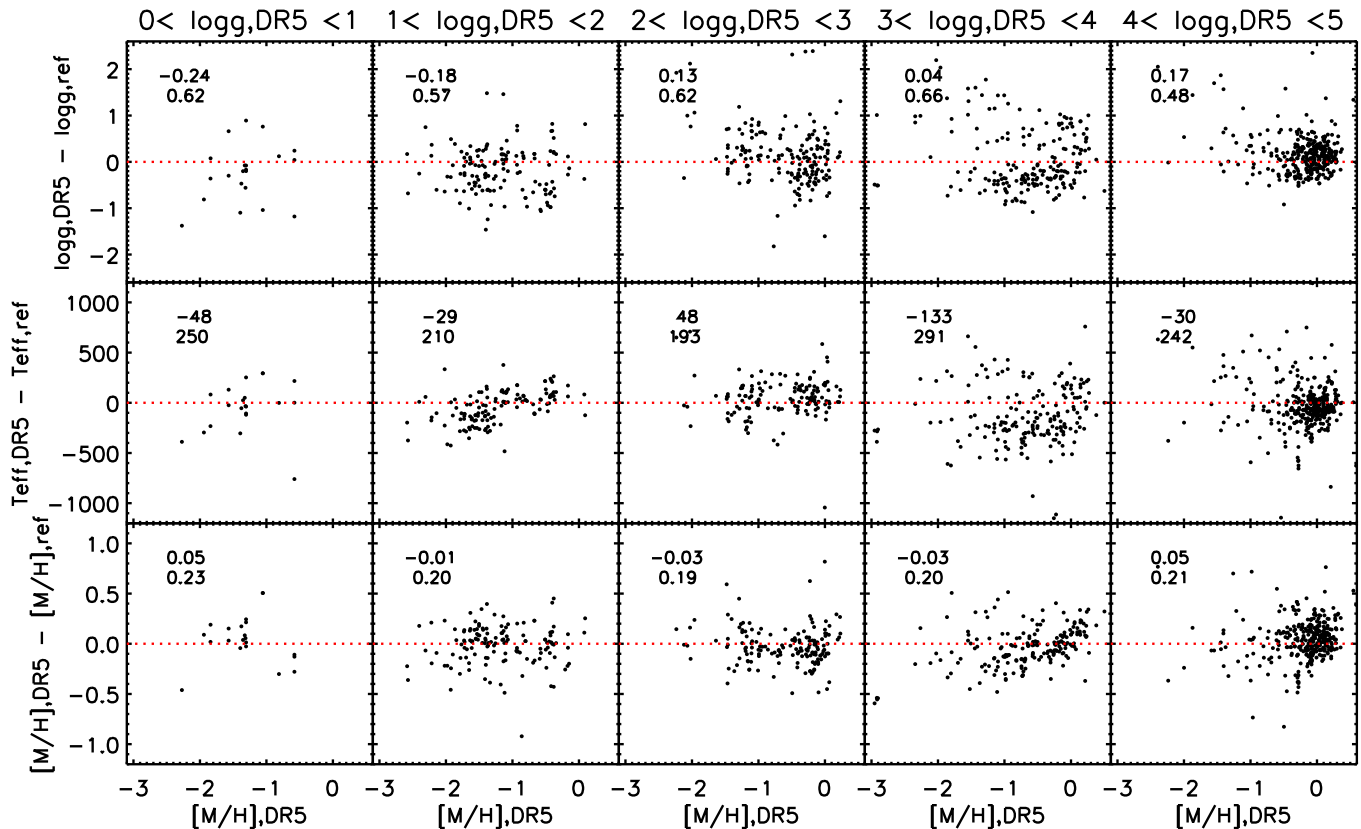


Figure 7. Residuals between the calibrated DR5 parameters and the reference values, as a function of the calibrated DR5 metallicity, for different calibrated DR5 $\log g$ bins. The numbers inside each panel indicate the mean difference (first line) and the dispersion (second line) for each considered subsample.

DR5 and DR4 values are very similar. Above $[M/H] \sim 0$, the DR5 metallicities are higher than the DR4 ones and are in better agreement with the chemical abundance pipeline presented below (Section 8). We note that after metallicity calibration we do not rerun the pipeline to see if other stellar parameters change with this new metallicity.

6.3. Surface Gravity Calibrations

Measuring the surface gravity spectroscopically, and in particular from medium-resolution spectra around the IR CaT, is challenging. Nevertheless, the DR4 pipeline proved to perform in a relatively reliable manner, so no calibration was performed on $\log g_p$. The uncertainties in the DR4 $\log g_p$ values are of the order of ~ 0.2 – 0.3 dex, with any offsets being mainly confined to the giant stars. In particular, an offset in $\log g_p$ of ~ 0.15 was detected for the red clump stars.

For the main DR5 catalog, the surface gravities are calibrated using both the asteroseismic $\log g$ values of 72 giants from V17 and the *Gaia* benchmark dwarfs and giants (Heiter et al. 2015). Although the calibration presented in V17 focuses only on giant stars and should therefore perform better for these stars (see Section 11), the global DR5 $\log g$ calibration is valid for all stars for which the stellar parameter pipeline provides T_{eff} , $\log g$, and $[M/H]$.

Biases in $\log g_p$ depended mostly on $\log g_p$, so for the surface gravity calibration, we computed the offset between the pipeline output and the reference values, as a function of the pipeline output, and a low-order polynomial fitted to the residuals (see V17 for a more quantitative assessment). This

quadratic expression defines our surface gravity calibration:

$$\log g_{\text{DR5}} = \log g_p - (-0.515 + 0.026 \log g_p + 0.023 \log g_p^2). \quad (3)$$

The calibration above affects mostly the giants but also allows a smooth transition of the calibration for the dwarfs. The red clump is now at $\log g \sim 2.5$ dex, consistent with isochrones for thin disk stars of metallicity $[M/H] = -0.1$ and age 7.5 Gyr (see Section 6.5). This calibration has the effect of increasing the minimum published $\log g$ from 0 (as set by the learning grid) to ~ 0.5 . The maximum reachable $\log g$ is ~ 5.2 (instead of 5.5, as in DR4). Tests carried out with the Galaxia model (Sharma et al. 2011), where the RAVE selection function has been applied (W16), show that the calibration improves $\log g$ even at these boundaries. We do caution, however, that special care should be taken for stars with $\log g \lesssim 0.75$ or $\log g \gtrsim 5$.

6.4. Effective Temperature Calibrations

Munari et al. (2014) showed that the DR4 effective temperatures for warm stars ($T_{\text{eff}} \gtrsim 6000$ K) are underestimated by ~ 250 K. This offset is evident when plotting the residuals against the reference (photometric) T_{eff} , but is barely discernible when plotting them against the pipeline T_{eff} . Consequently, it is difficult to correct for this effect. The calibration that we carry out changes $T_{\text{eff,p}}$ only modestly, and does not fully compensate for the (fortunately small) offsets (see Figure 6). The adopted calibration for effective

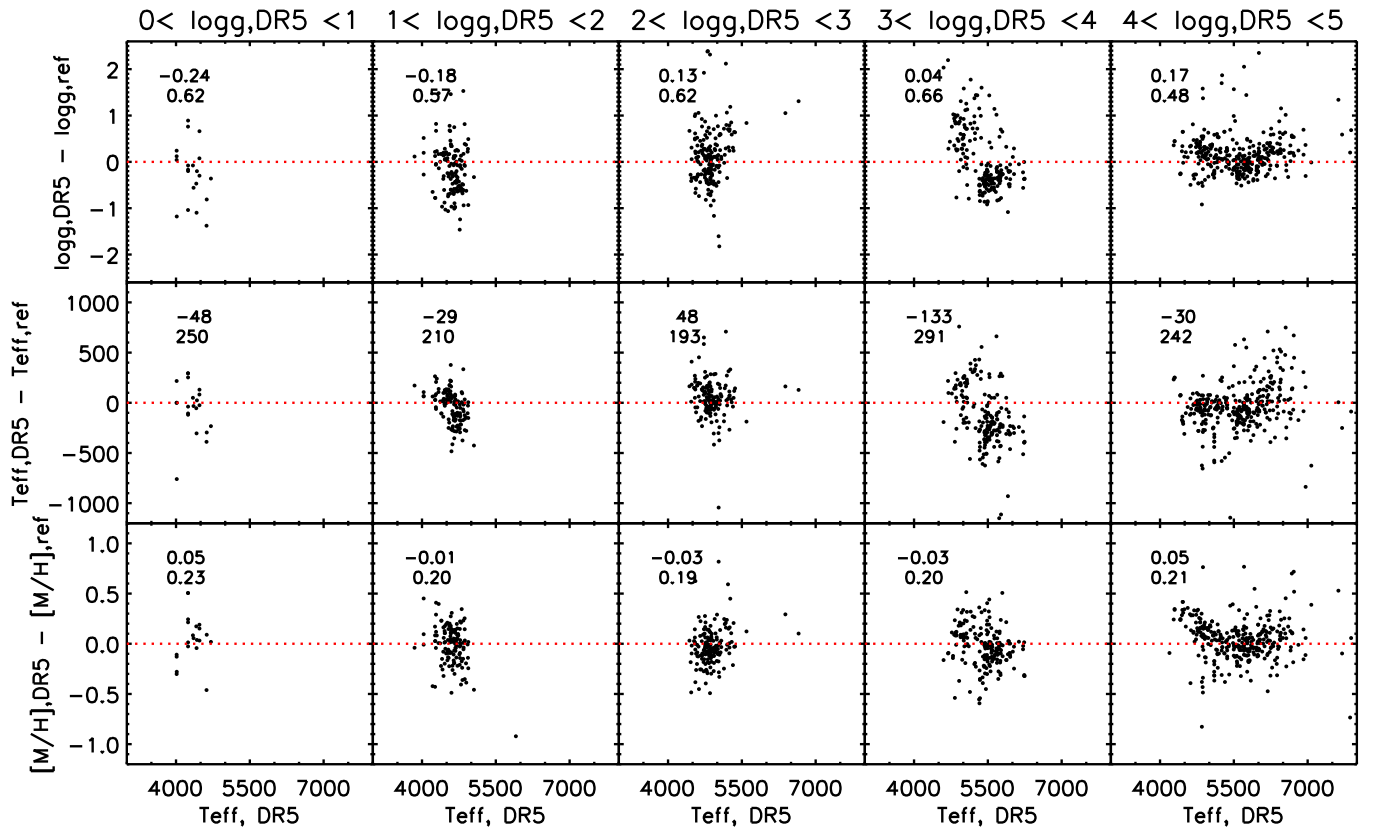


Figure 8. Same as Figure 7, but showing on the x-axis the calibrated DR5 T_{eff} .

temperatures is

$$T_{\text{eff,DR5}} = T_{\text{eff,p}} + (285 - 0.073T_{\text{eff,p}} + 40 \log g_p). \quad (4)$$

6.5. Summary of the Calibrations

Figures 7 and 8 show, as functions of metallicity and effective temperature respectively, the residuals between the calibrated values and the set of reference stars that have been used. We show the $\log g$ comparison (first rows of Figures 7 and 8) for all sets of stars, and not only the stars in V17 and Jofré et al. (2014), which in the end were the only samples used to define the calibration. Although the derivations of $\log g$ in V17 and Jofré et al. (2014) are independent of each other, the shifts in $\log g$ between the two samples are small, so there is no concern that we could end up with nonphysical combinations of parameters.

Overall there are no obvious trends as a function of any stellar parameter, except the already mentioned mild trend in T_{eff} for the stars having $4 < \log g < 5$ (seen in the middle row, last column of Figure 8). The absence of any strong bias in the parameters is also confirmed in the next sections, with additional comparisons with APOGEE, *Gaia*-ESO, and LAMOST stars (Section 7).

The effect of the calibrations on the (T_{eff} , $\log g$) diagram is shown in Figure 9. The calibrations bring the distribution of stars into better agreement with the predictions of isochrones for the old thin disk and thick disk (yellow and red, respectively).

6.6. Estimation of the Atmospheric Parameter Errors and Robustness of the Pipeline

Using the error spectrum of each observation, 10 resampled spectra were computed for the entire database (see also Section 4). The SPARV algorithm was run on these spectra, the radial velocity estimated, and the spectra shifted to the rest frame. Subsequently, the pipeline of Kordopatis et al. (2013a) was run on these radial velocity-corrected spectra.

The dispersion of the derived parameters among the resampled spectra of each observation gives us an indication of the individual errors on T_{eff} , $\log g$, and $[M/H]$ and of the robustness of the pipeline. That said, because the noise is being introduced twice (once during the initial observation and once when resampling), the results should be considered as an overestimation of the errors (since we are dealing with an overall lower S/N).

Figure 10 shows the dispersion of each parameter determined from the spectra collected in 2006. We show both the simple standard deviation and the MAD estimator, which is more robust to outliers. The distribution of the internal errors (normalized to the peak of the black histogram) as given in Tables 1 and 2 of Kordopatis et al. (2013a) is also plotted. Figure 10 shows that the internal errors are consistent with the parameter dispersion we obtain from the resampled spectra, though the uncertainties calculated from the error spectra have a tail extending to larger error values. Therefore, for some stars, the true errors are considerably larger than those produced by the pipeline. This is not unexpected, as it reflects the degeneracies that hamper the IR CaT region, and also the fact

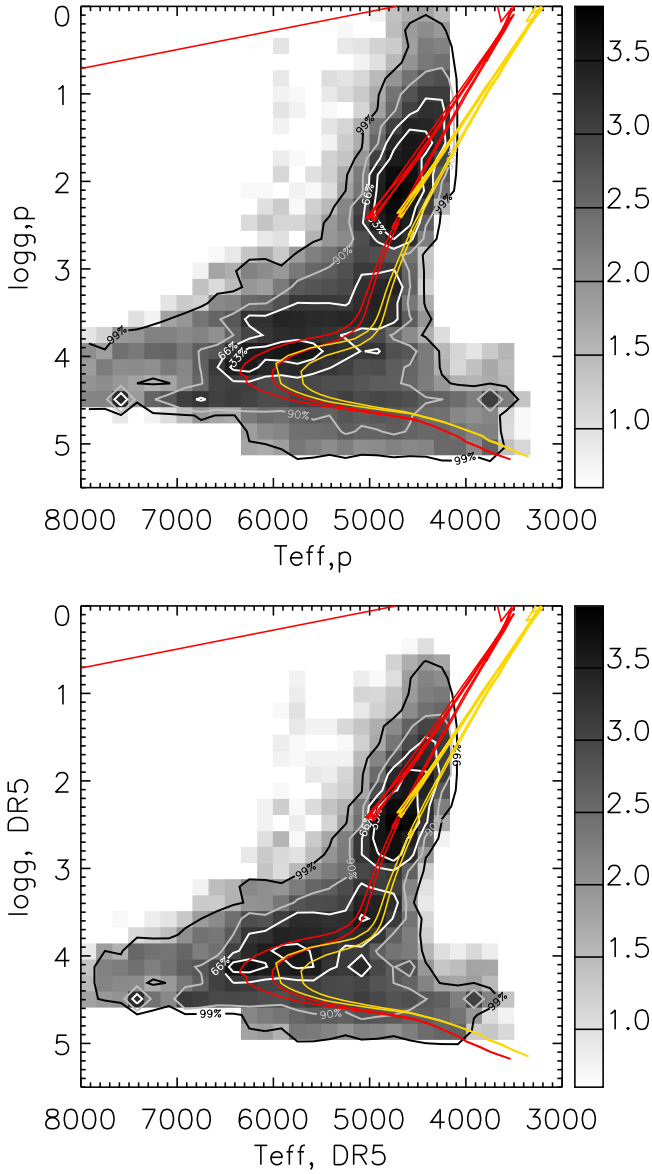


Figure 9. Top: $T_{\text{eff}}\text{-log } g$ diagram for the raw output of the pipeline, i.e., before calibration. Bottom: $T_{\text{eff}}\text{-log } g$ diagram for the calibrated DR5 parameters. Both plots show in red two Padova isochrones at metallicity -0.5 and ages 7.5 and 12.5 Gyr, and in yellow two Padova isochrones at metallicity -0.1 and ages 7.5 and 12.5 Gyr. For the new calibration, the locus of the red clump agrees better with stellar evolution models, as does the position of the turnoff.

that the resampled spectra have a lower S/N than the true observations, since the noise is introduced a second time.

The published DR5 parameters, however, are not the raw output of the pipeline, but are calibrated values. Since this calibration takes into account the output T_{eff} , $\log g$, and $[M/H]$, it is also valuable to test the dispersion of the calibrated values. This is shown in Figure 11 for the same set of stars. As before, no large differences are introduced, indicative again of a valid calibration and reliable stellar parameter pipeline.

6.7. Completeness of Stellar Parameters

It is of value to consider the completeness of DR5 with respect to derived stellar parameters. To evaluate this, the stars that satisfy the following criteria are selected: $S/N \geq 20$,

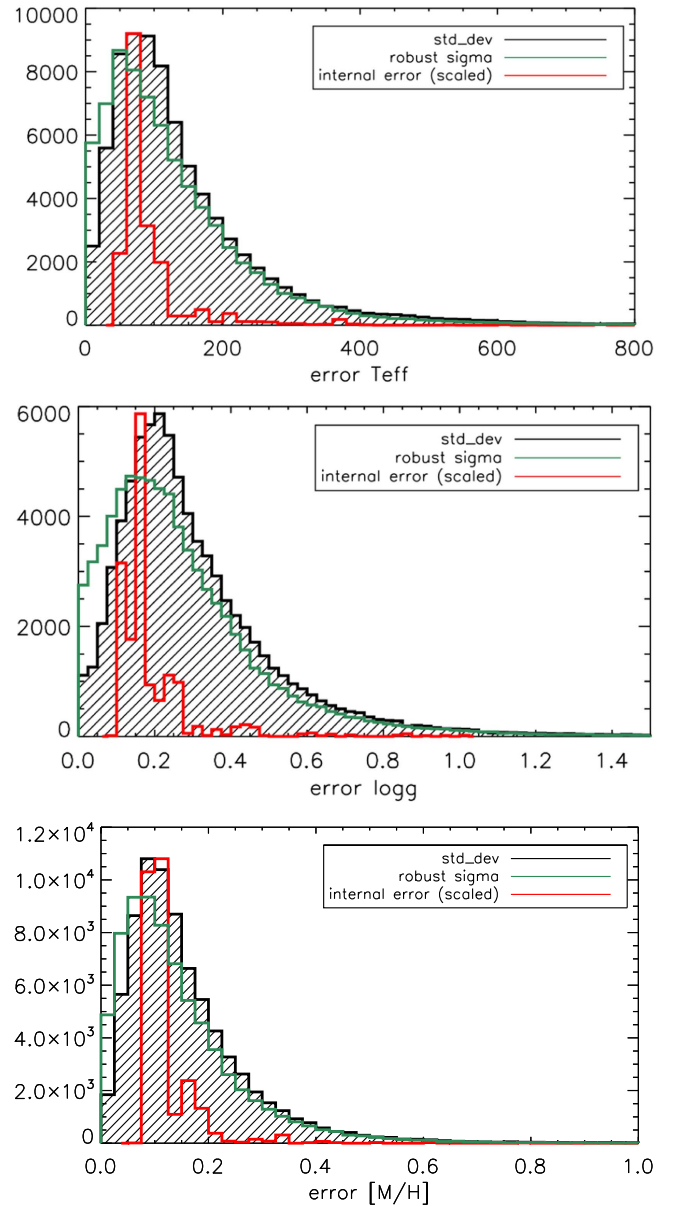


Figure 10. Histograms of the errors in the uncalibrated parameters (top: T_{eff} , middle: $\log g$, bottom: $[M/H]_p$), obtained from the analysis of all the spectra gathered in 2006, resampled 10 times using their associated error spectra. The filled black histograms show the standard deviation distributions whereas green histograms show the MAD estimator distribution. The red histograms are normalized to the peak of the standard deviation distribution and show the distributions of the internal errors as estimated by the stellar parameter pipeline.

$|\text{correctionRV}| < 10 \text{ km s}^{-1}$, $\sigma(\text{RV}) < 8 \text{ km s}^{-1}$, and $\text{correlationCoeff} > 10$ (see Kordopatis et al. 2013a). The resulting distributions are shown in Figure 12. Whereas the magnitude bin $10.0 < I_{2\text{MASS}} < 10.8$ has the highest number of stars with spectral parameters, distances, and chemical abundances, the fractional completeness compared to 2MASS (bottom left panel) peaks in the magnitude bin $9.0 < I_{2\text{MASS}} < 10.0$. In this bin, we find that we determine stellar parameters for approximately 50% of 2MASS stars in the RAVE fields. We further estimate distances for 40% of stars, and chemical abundances for $\sim 20\%$. This fraction drops off significantly at fainter magnitudes.

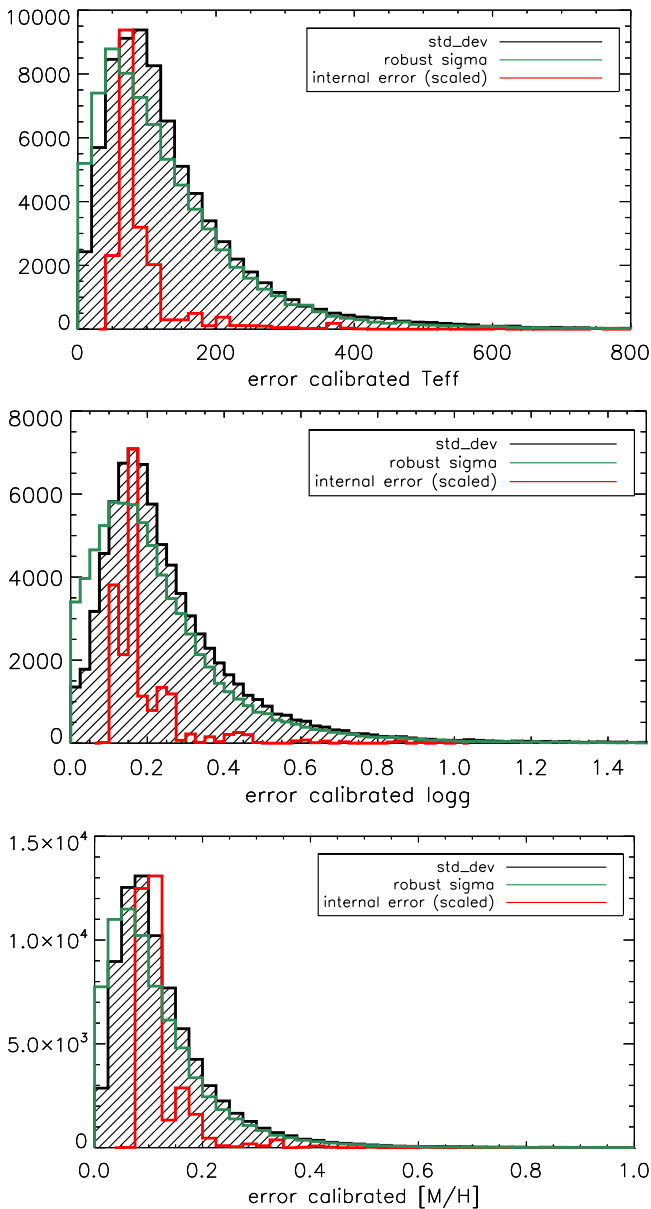


Figure 11. Same as Figure 10 but showing the error histograms for the calibrated DR5 parameters.

Similarly, for the brighter bins we obtain stellar parameters for $\sim 55\%$ of Tycho-2 stars, distances for $\sim 45\%$ of stars, and similar trends in the completeness fraction of chemical abundances.

7. EXTERNAL VERIFICATION

Stars observed specifically for understanding the stellar parameters of RAVE, as well as stars observed that fortuitously overlap with high-resolution studies, are compiled to further assess the validity of the RAVE stellar parameter pipeline. As discussed above, calibrating the RAVE stellar parameter pipeline is not straightforward, and although a global calibration over the diverse RAVE stellar sample has been applied, the accuracy of the atmospheric parameters depends also on the stellar population probed. Therefore, for the specific samples investigated in this section, Table 4 summarizes the

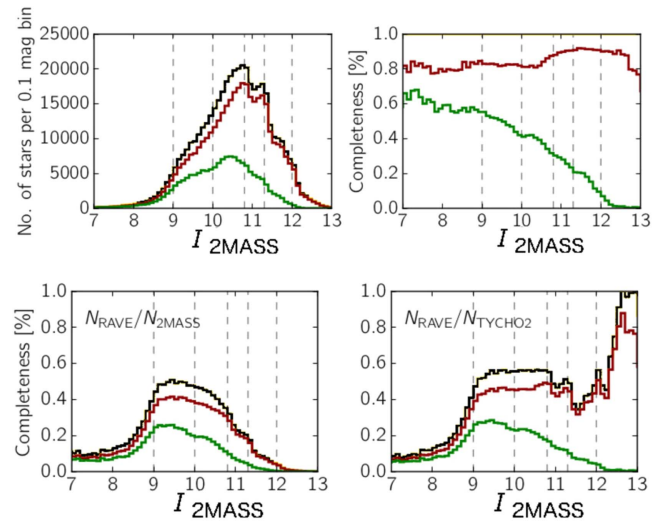


Figure 12. Top left panel: the number of RAVE stars with spectral parameters (black), distances (red), and chemical abundances (green) as a function of magnitude. Top right panel: the completeness of the RAVE DR5 sample is shown as a function of magnitude for stars with spectral parameters, distances, and chemical abundances. Bottom left panel: the completeness of the RAVE DR5 sample with respect to the completeness of 2MASS is shown as a function of magnitude for stars with spectral parameters, distances and chemical abundances. Bottom right panel: the same as the bottom left panel, but for Tycho-2.

results of the external comparisons split into (i) hot, metal-poor dwarfs, (ii) hot, metal-rich dwarfs, (iii) cool, metal-poor dwarfs, (iv) cool, metal-rich dwarfs, (v) cool, metal-poor giants, and (vi) cool, metal-rich giants. The boundary between “metal-poor” and “metal-rich” occurs at $[M/H] = -0.5$, and that between “hot” and “cool” lies at $T_{\text{eff}} = 5500$ K. The giants and dwarfs are divided at $\log g = 3.5$ dex. From here on, only the calibrated RAVE stellar parameters are used.

7.1. Cluster Stars

In the 2011B, 2012, and 2013 RAVE observing semesters, stars in various open and globular clusters were targeted with the goal of using the cluster stars as independent checks on the reliability of RAVE stellar parameters and their errors. RAVE stars observed within the targeted clusters that have also been studied externally from high-resolution spectroscopy are compiled, so a quantitative comparison of the RAVE stellar parameters can be made.

Table 3 lists clusters and their properties for which RAVE observations could be matched to high-resolution studies. The properties of open clusters come from the Milky Way global survey of star clusters (Kharchenko et al. 2013) and the properties of globular clusters come from the Harris catalog (Harris 1996, 2010 update). The number of RAVE stars that were crossmatched and the literature sources are also listed.

Figure 13 shows a comparison between the high-resolution cluster studies and the RAVE cluster stars. From this inhomogeneous sample of 75 overlap RAVE cluster stars with an $\text{AlgoConv} \neq 1$, the formal uncertainties in T_{eff} , $\log g$, and $[M/H]$ are 300 K, 0.6 dex, and 0.04 dex, respectively, but decrease by a factor of almost two when only stars with

Table 3
RAVE Targeted Clusters

Cluster ID	Alternative Name	R.A.	Decl.	Ang. Rad. (deg)	RV_{helio}	[Fe/H]	Dist. (kpc)	Age (Gyr)	Semester Targeted	Total # RAVE (AlgoConv = 0)	Comments
Pleiades	Melotte 22, M45	03 47 00	24 07 00	6.2	5.5	-0.036	0.130	0.14	2011B	11 (8)	Funayama et al. (2009)
Hyades	Melotte 25	04 26 54	15 52 00	20	39.4	0.13	0.046	0.63	2011B	5 (5)	Takeda et al. (2013)
IC 4651	...	17 24 49	-49 56 00	0.24	-31.0	-0.102	0.888	1.8	2011B	10 (4)	Carretta et al. (2014), Pasquini et al. (2004)
47 Tuc ^{GC}	NGC 104	00 24 05	-72 04 53	0.42	-18.0	-0.72	4.5	13	2012B	23 (12)	Cordero et al. (2014), Koch & McWilliam (2008), Carretta et al. (2009)
NGC 2477	M93	07 52 10	-38 31 48	0.45	7.3	-0.192	1.450	0.82	2012B	9 (4)	Bragaglia et al. (2008), Mishenina et al. (2015)
M67	NGC 2682	08 51 18	11 48 00	1.03	33.6	-0.128	0.890	3.4	2012A + 2013	1 (1)	Önehag et al. (2014)
Blanco 1	...	00 04 07	-29 50 00	2.35	5.5	0.012	0.250	0.06	2013	1 (1)	Ford et al. (2005)
Omega Cen ^{GC}	NGC 5139	09 12 03.10	-64 51 48.6	0.12	101.6	-1.14	9.6	10	2013	15 (2)	Johnson & Pilachowski (2010)
NGC 2632	Praesepe	08 40 24.0	+19 40 00	3.1	33.4	0.094	0.187	0.83	2012	1 (0)	Yang et al. (2015)

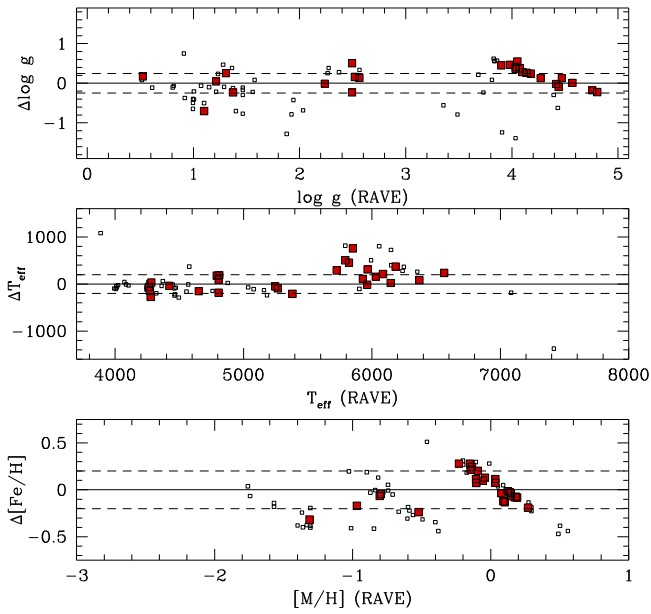


Figure 13. Comparison between the stellar parameters presented here and those from cluster stars studied in the literature from various different sources (see Table 3). The filled squares indicate the stars with $\text{AlgoConv} = 0$.

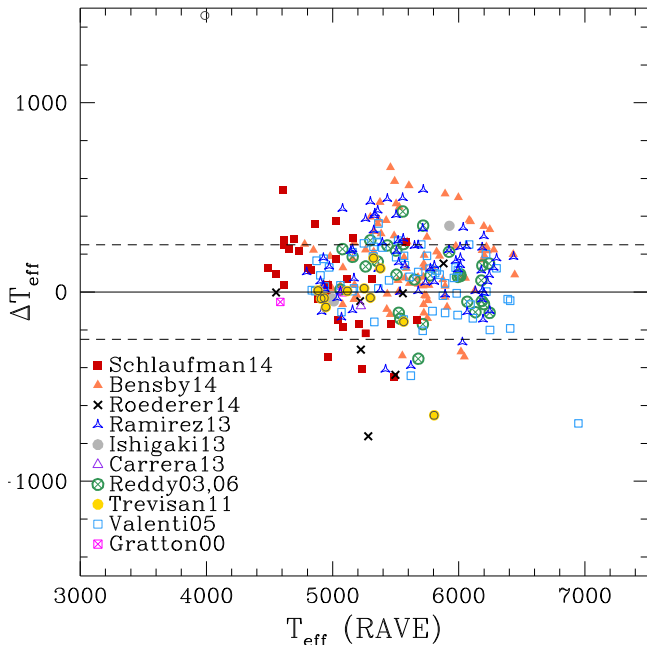


Figure 14. Comparison between the T_{eff} presented here and those from field stars studied using high-resolution studies in the literature from various different sources. Stars shown are only those with $\text{AlgoConv} = 0$ and T_{eff} between 4000 and 8000 K.

$S/N > 50$ are considered (see Table 5). This is a $\sim 15\%$ improvement on the same RAVE cluster stars in DR4.

7.2. Field Star Surveys

We have matched RAVE stars with the high-resolution studies of Gratton et al. (2000), Carrera et al. (2013), Ishigaki et al. (2013), Roederer et al. (2014), and Schlafman & Casey (2014), which concentrate on bright, metal-poor stars, the study of Trevisan et al. (2011), which concentrates on old, metal-rich stars, and the studies of Ramírez et al. (2013), Reddy et al.

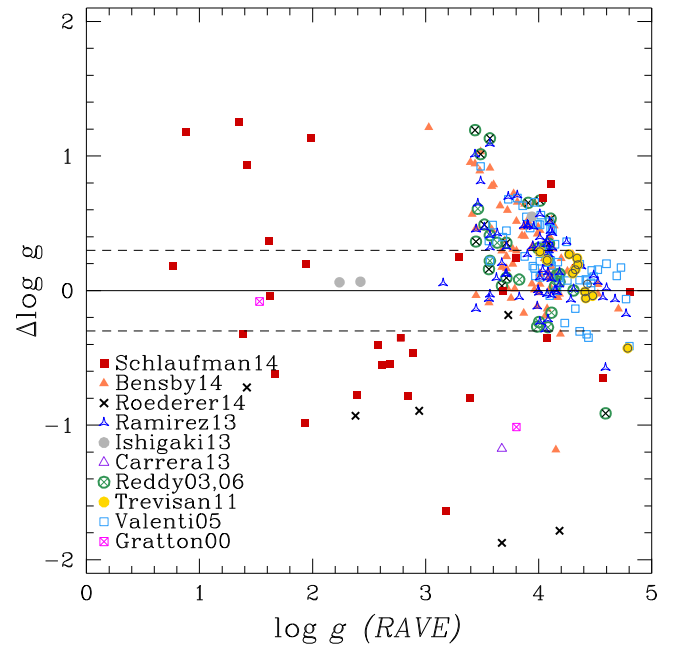


Figure 15. Comparison between the $\log g$ presented here and those from field stars studied using high-resolution studies in the literature from various different sources. Stars shown are only those with $\text{AlgoConv} = 0$ and T_{eff} between 4000 and 8000 K.

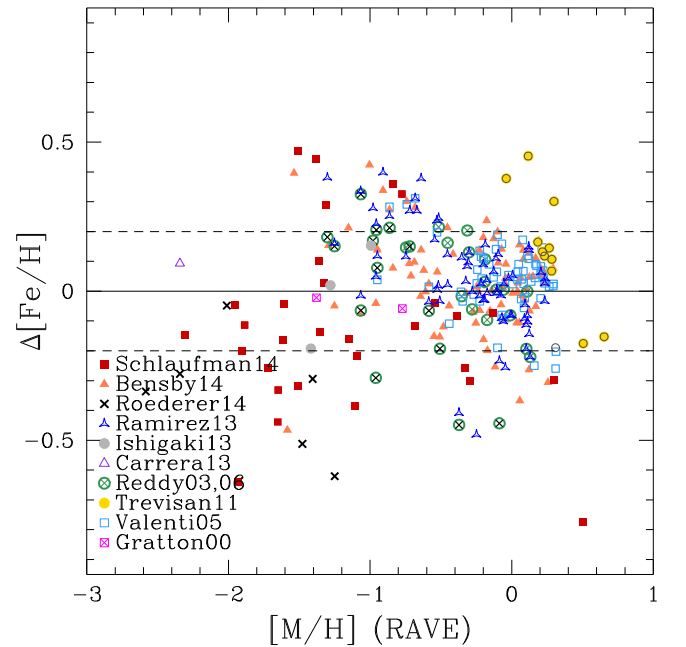


Figure 16. Comparison between the $[\text{Fe}/\text{H}]$ presented here and those from field stars studied using high-resolution studies in the literature from various different sources. Stars shown are only those with $\text{AlgoConv} = 0$ and T_{eff} between 4000 and 8000 K.

(2003, 2006), Valenti & Fischer (2005), and Bensby et al. (2014), which target FGK stars in the solar neighborhood. Figures 14–16 compare stellar parameters from these studies with the DR5 values. Trends are detectable in $\log g$ for both giants and dwarfs. For the giants the same tendency for $\log g$ to be overestimated when it $\log g$ is small was evident in V17. In Figure 15 a similar, but less pronounced, tendency is evident in the $\log g$ values for dwarfs.

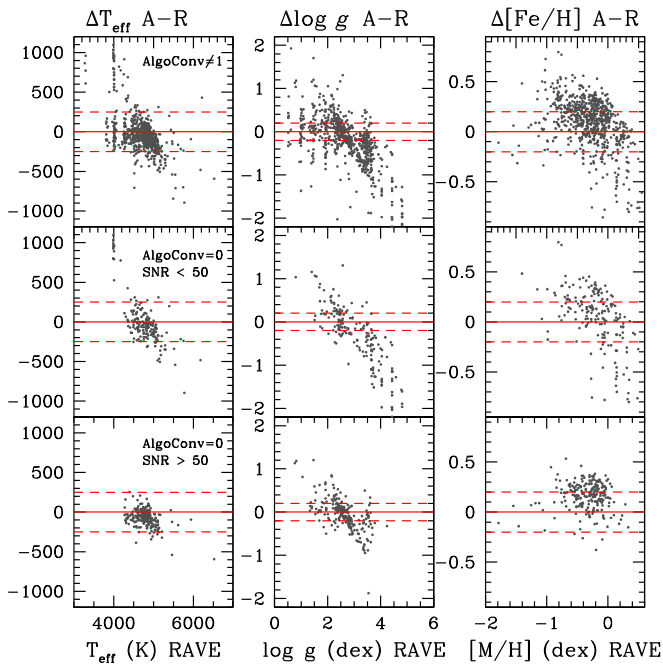


Figure 17. Comparison between the stellar parameters of the RAVE stars that overlap with APOGEE. Different subsets of S/N and *AlgoConv* cuts are shown.

7.3. APOGEE

The Apache Point Observatory Galactic Evolution Experiment, part of the Sloan Digital Sky Survey and covering mainly the Northern Hemisphere, has made public near-IR spectra with a resolution of $R \sim 22,500$ for over 150,000 stars (DR12, Holtzman et al. 2015). Stellar parameters are provided only for APOGEE giant stars, and temperatures, gravities, [Fe/H] metallicities, and radial velocities are reported to be accurate to ~ 100 K (internal), ~ 0.11 dex (internal), ≤ 0.1 dex (internal), and ~ 100 m s $^{-1}$, respectively (Holtzman et al. 2015; Nidever et al. 2012). Despite the different hemispheres targeted by RAVE and APOGEE, there are ~ 1100 APOGEE stars that overlap with RAVE DR5 stars, two-thirds of these having valid APOGEE stellar parameters.

A comparison between the APOGEE and RAVE stellar parameters is shown in Figure 17. The zero-point and standard deviation for different subsets of S/N and *AlgoConv* are provided in Table 5. There appears to be a ~ 0.15 dex zero-point offset in [Fe/H] between APOGEE and RAVE, as seen most clearly in the high S/N sample, and there is a noticeable break in $\log g$ where the cool main-sequence stars and stars along the giant branch begin to overlap. This is a consequence of degeneracies in the CaT region that affect the determination of $\log g$ (see Tables 1 and 2 in DR4).

7.4. LAMOST

The Large sky Area Multi-Object Spectroscopic Telescope is an ongoing optical spectroscopic survey with a resolution of $R \sim 1800$, and has gathered spectra for more than 4.2 million objects. About 2.2 million stellar sources, mainly with S/N > 10 , have stellar parameters. Typical uncertainties are 150 K, 0.25 dex, 0.15 dex, and 5 km s $^{-1}$ for T_{eff} , $\log g$, metallicity, and radial velocity, respectively (Xiang et al. 2014).

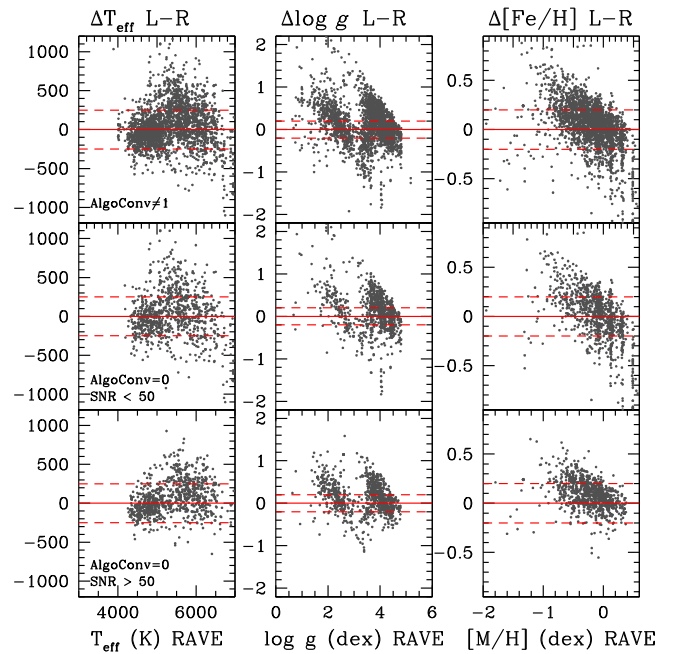


Figure 18. Comparison between the stellar parameters of the stars presented here and those from LAMOST. There are 2700, 1026, and 987 stars in the top, middle, and bottom panels, respectively.

The overlap between LAMOST and RAVE comprises almost 3000 stars, including both giants and dwarfs. Figure 18 shows the comparison between the stellar parameters of RAVE and LAMOST. The giants (stars with $\log g < 3$) and dwarfs (stars with $\log g > 3$) exhibit different trends in $\log g$, and the largest uncertainties in $\log g$ occur where these populations overlap in $\log g$. The zero-point and standard deviation for the comparisons between RAVE and LAMOST stellar parameters are provided in Table 4.

7.5. GALAH

The GALAH Survey is a high-resolution ($R \sim 28,000$) spectroscopic survey using the HERMES spectrograph and Two Degree Field fiber positioner on the 3.9 m Anglo-Australian telescope. The first data release provides T_{eff} , $\log g$, $[\alpha/\text{Fe}]$, radial velocity, distance modulus, and reddening for 9860 Tycho-2 stars (Martell et al. 2016). There are ~ 1800 RAVE stars that overlap with a star observed in GALAH, spanning the complete range in temperature, gravity, and metallicity.

Figure 19 shows the comparison of stellar parameters between the RAVE and Galah overlap stars, and Table 4 quantifies the agreement between these two surveys.

7.6. GAIA-ESO

Gaia-ESO, a public spectroscopic survey observing stars in all major components of the Milky Way using the Very Large Telescope, provides 14,947 unique targets in DR2. The resolution of the stellar spectra ranges from $R \sim 17,000$ to $R \sim 47,000$. There are ~ 100 RAVE stars that overlap with a star observed in *Gaia*-ESO; half of these are situated around the η Chamaeleontis Cluster (Mamajek et al. 1999), and a third are in the vicinity of the γ Velorum cluster (Jeffries et al. 2014). The overlap sample is small and new internal values are being

Table 4
Estimates of the External Errors in the Stellar Parameters

Stellar type	N	$\sigma(T_{\text{eff}})$	$\sigma(\log g)$	$\sigma([M/H])$	$\sigma(T_{\text{eff,IRFM}})$
Dwarfs ($\log g > 3.5$)					
Hot, all metallicities DR5	375	442	0.39	0.41	129
Hot, metal-poor DR5	38	253	0.48	0.95	258
Hot, metal-rich DR5	337	453	0.38	0.95	233
Cool, all metallicities DR5	332	250	0.75	0.41	187
Cool, metal-poor DR5	68	303	0.87	0.61	301
Cool, metal-rich DR5	264	233	0.72	0.29	146
S/N > 40					
Hot, all metallicities RAVE-on	510	411	0.56	0.37	...
Hot, metal-poor RAVE-on	95	498	0.94	0.55	...
Hot, metal-rich RAVE-on	415	389	0.41	0.32	...
Cool, all metallicities RAVE-on	267	291	0.62	0.24	...
Cool, metal-poor RAVE-on	49	417	0.75	0.32	...
Cool, metal-rich RAVE-on	218	255	0.57	0.20	...
S/N > 40					
Hot, all metallicities DR5	260	210	0.29	0.16	...
Hot, metal-poor DR5	30	260	0.39	0.16	...
Hot, metal-rich DR5	230	201	0.28	0.15	...
Cool, all metallicities	185	202	0.50	0.17	...
Cool, metal-poor	48	256	0.70	0.21	...
Cool, metal-rich	137	164	0.41	0.13	...
S/N > 40					
Hot, all metallicities RAVE-on	314	273	0.34	0.21	...
Hot, metal-poor RAVE-on	55	354	0.61	0.36	...
Hot, metal-rich RAVE-on	259	253	0.24	0.16	...
Cool, all metallicities RAVE-on	187	250	0.54	0.17	...
Cool, metal-poor RAVE-on	35	303	0.65	0.21	...
Cool, metal-rich RAVE-on	152	237	0.49	0.15	...
Giants ($\log g < 3.5$)					
All, all metallicities DR5	1294	156	0.48	0.17	110
Hot DR5	28	240	0.45	0.30	261
Cool, metal-poor DR5	260	211	0.58	0.20	93
Cool, metal-rich DR5	1006	125	0.46	0.15	96
S/N > 40					
All, all metallicities RAVE-on	1318	140	0.41	0.20	...
Hot RAVE-on	5	270	0.62	0.27	...
Cool, metal-poor RAVE-on	293	195	0.55	0.27	...
Cool, metal-rich RAVE-on	1020	110	0.36	0.17	...
S/N > 40					
Hot DR5	22	189	0.46	0.24	...
Cool, metal-poor DR5	225	210	0.58	0.20	...
Cool, metal-rich DR5	843	113	0.44	0.13	...
S/N > 40					
Hot RAVE-on	3	120	0.28	0.23	...
Cool, metal-poor RAVE-on	248	159	0.52	0.23	...
Cool, metal-rich RAVE-on	810	88	0.33	0.15	...
Giants (asteroseismically calibrated sample)					
All, all metallicities	N_g	$\sigma(T_{\text{eff,IRFM}})$	$\sigma(\log g_s)$	$\sigma([Fe/H]_c)$	
All, all metallicities	332	169	0.37	0.21	
Hot	11	640	0.39	0.28	
Cool, metal-poor	180	161	0.40	0.23	
Cool, metal-rich	835	107	0.29	0.15	
S/N > 40					
Hot	5	471	0.42	0.15	
Cool, metal-poor	154	170	0.38	0.21	
Cool, metal-rich	701	95	0.28	0.12	

Table 5
RAVE External Comparisons By Survey

	AlgoConv \neq 1		AlgoConv = 0, S/N < 50		AlgoConv = 0, S/N > 50	
APOGEE	T_{eff} :	-30 ± 277	T_{eff} :	4 ± 342	T_{eff} :	-75 ± 107
	$\log g$:	-0.22 ± 0.60	$\log g$:	-0.35 ± 0.70	$\log g$:	-0.05 ± 0.37
	[Fe/H]:	0.08 ± 0.44	[Fe/H]:	0.05 ± 0.52	[Fe/H]:	0.16 ± 0.14
	Num:	711	Num:	190	Num:	221
	$\log g_{\text{sc}}$:	0.03 ± 0.29	$\log g_{\text{sc}}$:	0.06 ± 0.31	$\log g_{\text{sc}}$:	0.00 ± 0.27
	Num _{sc} :	317	Num _{sc} :	129	Num _{sc} :	184
Gaia-ESO	T_{eff} :	243 ± 477	T_{eff} :	613 ± 659	T_{eff} :	52 ± 266
	$\log g$:	-0.12 ± 0.89	$\log g$:	-0.82 ± 0.91	$\log g$:	0.08 ± 0.46
	[Fe/H]:	0.25 ± 0.93	[Fe/H]:	-0.10 ± 0.30	[Fe/H]:	0.13 ± 0.21
	Num:	53	Num:	11	Num:	28
	$\log g_{\text{sc}}$:	0.17 ± 0.64	$\log g_{\text{sc}}$:	0.19 ± 0.35	$\log g_{\text{sc}}$:	0.16 ± 0.69
	Num _{sc} :	18	Num _{sc} :	3	Num _{sc} :	15
Clusters	T_{eff} :	38 ± 309	T_{eff} :	-62 ± 422	T_{eff} :	106 ± 244
	$\log g$:	-0.12 ± 0.63	$\log g$:	-0.42 ± 1.13	$\log g$:	0.13 ± 0.29
	[Fe/H]:	-0.10 ± 0.28	[Fe/H]:	-0.21 ± 0.39	[Fe/H]:	0.01 ± 0.16
	Num:	75	Num:	15	Num:	26
	$\log g_{\text{sc}}$:	-0.39 ± 0.45	$\log g_{\text{sc}}$:	-0.59 ± 0.29	$\log g_{\text{sc}}$:	-0.17 ± 0.50
	Num _{sc} :	14	Num _{sc} :	6	Num _{sc} :	7
Misc. Field Stars	T_{eff} :	126 ± 397	T_{eff} :	251 ± 517	T_{eff} :	111 ± 196
	$\log g$:	-0.05 ± 0.95	$\log g$:	-0.33 ± 1.17	$\log g$:	0.15 ± 0.51
	[Fe/H]:	-0.09 ± 0.40	[Fe/H]:	-0.17 ± 0.48	[Fe/H]:	0.01 ± 0.18
	Num:	317	Num:	57	Num:	169
	$\log g_{\text{sc}}$:	-0.25 ± 0.90	$\log g_{\text{sc}}$:	-0.37 ± 0.95	$\log g_{\text{sc}}$:	-0.18 ± 0.90
	Num _{sc} :	51	Num _{sc} :	16	Num _{sc} :	33
LAMOST	T_{eff} :	30 ± 325	T_{eff} :	-4 ± 364	T_{eff} :	58 ± 208
	$\log g$:	0.12 ± 0.48	$\log g$:	0.08 ± 0.49	$\log g$:	0.16 ± 0.36
	[Fe/H]:	0.05 ± 0.27	[Fe/H]:	0.00 ± 0.27	[Fe/H]:	0.09 ± 0.15
	Num:	2700	Num:	2026	Num:	987
	$\log g_{\text{sc}}$:	0.14 ± 0.40	$\log g_{\text{sc}}$:	0.24 ± 0.45	$\log g_{\text{sc}}$:	0.06 ± 0.33
	Num _{sc} :	557	Num _{sc} :	224	Num _{sc} :	313
GALAH	T_{eff} :	-36 ± 274	T_{eff} :	-43 ± 376	T_{eff} :	-6 ± 144
	$\log g$:	0.0 ± 0.50	$\log g$:	-0.02 ± 0.59	$\log g$:	0.06 ± 0.35
	[Fe/H]:	-0.02 ± 0.33	[Fe/H]:	-0.07 ± 0.45	[Fe/H]:	0.04 ± 0.13
	Num:	1700	Num:	526	Num:	663
	$\log g_{\text{sc}}$:	0.04 ± 0.45	$\log g_{\text{sc}}$:	0.0 ± 0.56	$\log g_{\text{sc}}$:	0.06 ± 0.32
	Num _{sc} :	1255	Num _{sc} :	443	Num _{sc} :	613

analyzed currently; still Table 4 quantifies the results between these two surveys.

8. ELEMENTAL ABUNDANCES

The elemental abundances for aluminum, magnesium, nickel, silicon, titanium, and iron are determined for a number of RAVE stars using a dedicated chemical pipeline that relies on a library of equivalent widths encompassing 604 atomic and molecular lines in the RAVE wavelength range. This chemical pipeline was first introduced by Boeche et al. (2011) and then improved upon for the DR4 data release.

Briefly, equivalent widths are computed for a grid of stellar parameter values in the following ranges: T_{eff} from 4000 to 7000 K, $\log g$ from 0.0 to 0.5 dex, [M/H] from -2.5 to $+0.5$ dex, and five levels of abundances from -0.4 to $+0.4$ dex relative to the metallicity, in steps of 0.2 dex, using the solar abundances of Grevesse & Sauval (1998). Using the calibrated RAVE effective temperatures, surface gravities, and

metallicities (see Section 5), the pipeline searches for the best-fitting model spectrum by minimizing the χ^2 between the models and the observations.

The line list and specific aspects of the equivalent width library are given in Boeche et al. (2011) and the full scheme to compute the abundances is given in Section 5 of Kordopatis et al. (2013a). Abundances from the RAVE chemical abundance pipeline are provided only for stars fulfilling the following criteria:

1. T_{eff} must be between 4000 and 7000 K
2. $S/N > 20$
3. Rotational velocity, $V_{\text{rot}} < 50 \text{ km s}^{-1}$.

The highest quality of abundances will be determined for stars that satisfy the following additional constraints:

1. $\chi^2 < 2000$, where χ^2 quantifies the mismatch between the observed spectrum and the best-matching model.

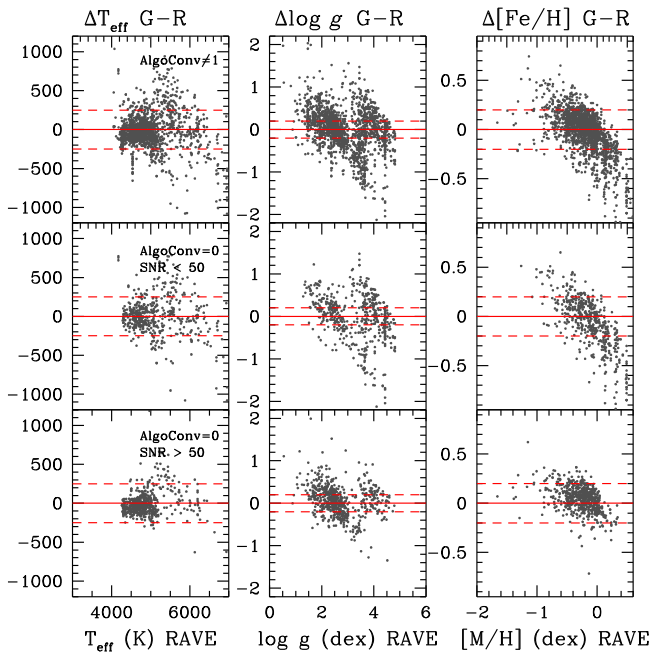


Figure 19. Comparison between the stellar parameters of the stars presented here and those from GALAH DR1.

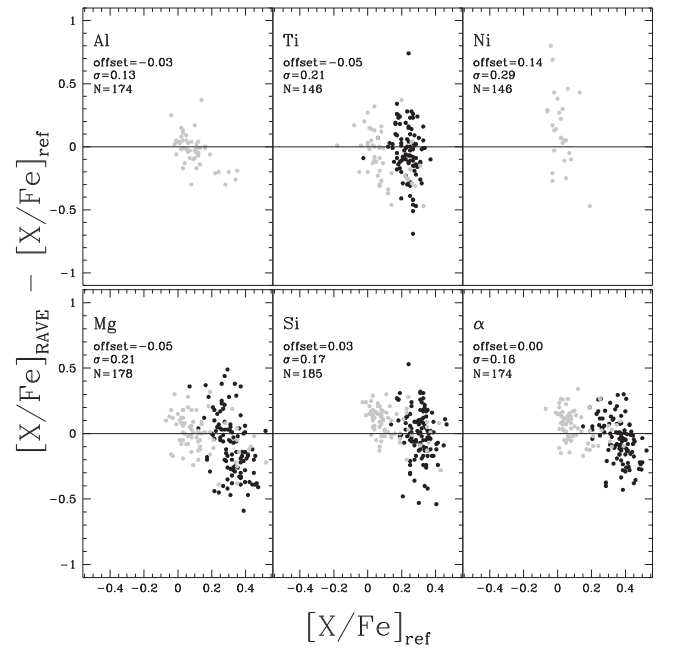


Figure 21. Comparison between the literature relative elemental abundance and residual abundances (RAVE minus literature). The stellar parameters and symbols used are as in Figure 20.

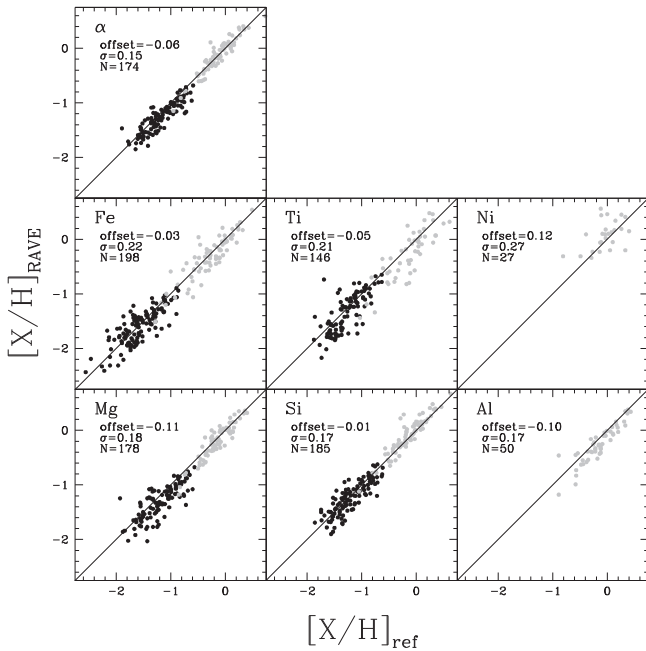


Figure 20. Comparison of high-resolution elemental abundances from Soubiran & Girard (2005) (gray) and Ruchti et al. (2011) (black) with the derived elemental abundances from the RAVE chemical pipeline. The input stellar parameters for the RAVE chemical pipeline are those presented here (see Section 5).

2. $\text{frac} > 0.7$, where frac represents the fraction of the observed spectrum that satisfactorily matches the model.
3. $c1$, $c2$ and $c3$ classification flags indicate that the spectrum is “normal” (see Matijević et al. 2012, for details on the classification flags).
4. AlgoConv value indicates the stellar parameter pipeline converged. $\text{AlgoConv} = 0$ indicates the highest quality result.

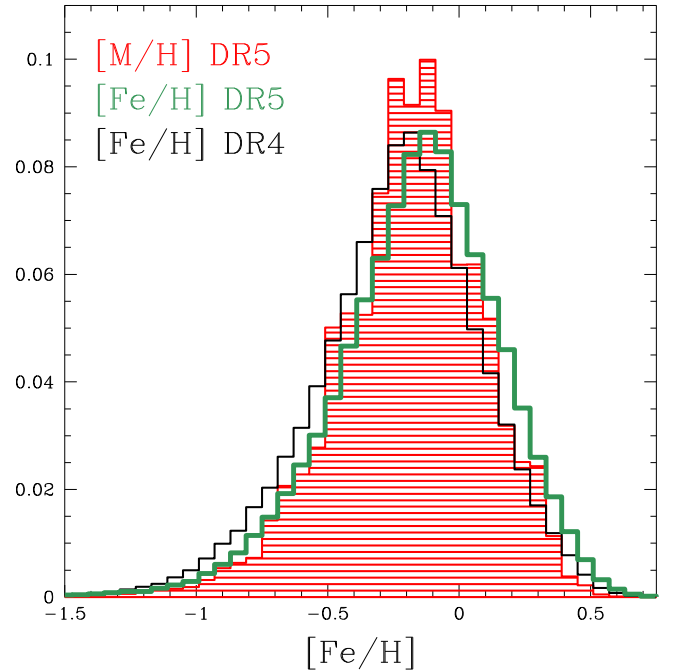


Figure 22. Comparison between the $[\text{Fe}/\text{H}]$ derived with the chemical pipeline and the calibrated $[\text{M}/\text{H}]$ values from the stellar parameter pipeline. Also shown is the $[\text{Fe}/\text{H}]$ distribution from DR4.

The precision and accuracy of the resulting elemental abundances are assessed in two ways. First, uncertainties in the elemental abundances are investigated from a sample of 1353 synthetic spectra. The typical dispersions are $\sigma \sim 0.05$ dex for $S/N = 100$ spectra, $\sigma \sim 0.1$ dex for $S/N = 40$ spectra and $\sigma \sim 0.25$ dex for $S/N = 20$ spectra. The exceptions are the element Fe, which has a smaller dispersion by a factor of two, and the element Ti, which has a larger dispersion

Table 6
Metallicities of the PARSEC v1.1 Isochrones Used

Z	Y	[M/H]
0.00010	0.249	-2.207
0.00020	0.249	-1.906
0.00040	0.249	-1.604
0.00071	0.250	-1.355
0.00112	0.250	-1.156
0.00200	0.252	-0.903
0.00320	0.254	-0.697
0.00400	0.256	-0.598
0.00562	0.259	-0.448
0.00800	0.263	-0.291
0.01000	0.266	-0.191
0.01120	0.268	-0.139
0.01300	0.272	-0.072
0.01600	0.277	0.024
0.02000	0.284	0.127
0.02500	0.293	0.233
0.03550	0.312	0.404
0.04000	0.320	0.465
0.04470	0.328	0.522
0.05000	0.338	0.581
0.06000	0.355	0.680

Note. We take and apply a scaled solar composition with $Y = 0.2485 + 1.78Z$.

by a factor of 1.5–2 (see Boeche et al. 2011; Kordopatis et al. 2013a, for details).

The number of measured absorption lines for an element, which is also provided in the DR5 data release, is, like S/N, a good indicator of the reliability of the abundance. The higher the number of measured lines, the better the expected precision. The relatively low uncertainty in the Fe abundances reflects the large number of its measurable lines at all stellar parameter values.

A second assessment of the performance of the chemical pipeline is provided by comparing the DR5 abundances in 98 dwarf stars with values given in Soubiran & Girard (2005) and in 203 giant stars with abundances in Ruchti et al. (2011). The dwarfs in Soubiran & Girard (2005) typically have RAVE S/N > 100, and the giants in Ruchti et al. (2011) have RAVE S/N in the range 30–90.

Figures 20 and 21 show the results obtained for the six elements from the RAVE chemical pipeline. In general, there is a slight improvement in the external comparisons from DR4, likely resulting from the improved DR5 calibration for the stellar parameters. The accuracy of the RAVE abundances depends on many variables, which can be interdependent in a nonlinear way, making it nontrivial to provide one value to quantify the accuracy of the RAVE elemental abundances. We also have not taken into account the errors in abundance measurements from high-resolution spectra. Here is a summary of the expected accuracy of the DR5 abundances, element by element.

1. *Magnesium*: The uncertainty is $\sigma_{\text{Mg}} \sim 0.2$ dex, slightly worse for stars with S/N < 40.
2. *Aluminum*: This is measured in RAVE spectra from only two isolated lines. Abundance errors are $\sigma_{\text{Al}} \sim 0.2$ dex, and slightly worse for stars with S/N < 40.
3. *Silicon*: This is one of the most reliably determined elements, with $\sigma_{\text{Si}} \sim 0.2$ dex, and slightly worse for stars with S/N < 40.

4. *Titanium*: The estimates are best for high-S/N, cool giants ($T_{\text{eff}} < 5500$ K and $\log g < 3$). We suggest rejecting Ti abundances for dwarf stars. Uncertainties for cool giants are $\sigma_{\text{Ti}} \sim 0.2$ dex, and slightly worse for stars with S/N < 40.
5. *Iron*: A large number of measurable lines are available at all stellar parameter values. The expected errors are $\sigma_{\text{Fe}} \sim 0.2$ dex.
6. *Nickel*: Ni estimates should be used for high-S/N, cool stars only ($T_{\text{eff}} < 5000$ K). In this regime, $\sigma_{\text{Ni}} \sim 0.25$ dex, but it correlates with the number of measured lines (i.e., with S/N).
7. *α -enhancement*: This is the average of [Mg/Fe] and [Si/Fe], and is a particularly useful measurement at low S/N. The expected uncertainty is $\sigma_{\alpha} \sim 0.2$ dex.

The green histogram in Figure 22 shows the distribution of [Fe/H] from the chemical pipeline. This is similar to the black histogram of [Fe/H] values in DR4 but shifted to slightly larger [Fe/H]. The red histogram of [M/H] values in DR5 is slightly narrower than either [Fe/H] histogram and peaks at slightly lower values than the DR5 [Fe/H] histogram.

9. DISTANCES, AGES, AND MASSES

In DR4 we included for the first time distances derived using the Bayesian method developed by Burnett & Binney (2010). This takes as its input the stellar parameters T_{eff} , $\log g$, and [M/H] determined from the RAVE spectra, and J , H , and K_s magnitudes from 2MASS. This method was extended by Binney et al. (2014), who included dust extinction in the modeling and introduced an improvement in the description of the distance to the stars by providing multi-Gaussian fits to the full probability density function (pdf) in distance modulus. Previous data releases included distance estimates from different sources (Breddels et al. 2010; Zwitter et al. 2010), but the Bayesian pipeline has been shown to be more robust when dealing with atmospheric parameter values with large uncertainties, so it provided the recommended distance estimates for DR4 and the only estimates that we provide with DR5.

We provide distance estimates for all stars except those for which we do not believe we can find reliable distances, which include stars with the following DR5 characteristics:

1. $\text{AlgoConv} = 1$ or S/N < 20,
2. $T_{\text{eff}} < 4000$ K and $\log g > 3.5$ (i.e., cool dwarfs), and
3. $T_{\text{eff}} > 7400$ K and [M/H] < -1.2.

The distance pipeline applies the simple Bayesian statement

$$P(\text{model}|\text{data}) = \frac{P(\text{data}|\text{model})P(\text{model})}{P(\text{data})},$$

where in our case “data” refers to the inputs described above for a single star, and “model” comprises a star of specified initial mass \mathcal{M} , age τ , metallicity [M/H], and location, observed through a specified line-of-sight extinction. $P(\text{data}|\text{model})$ is determined assuming uncorrelated Gaussian uncertainties on all inputs, and using isochrones to find the values of the stellar parameters and absolute magnitudes of the model star. The uncertainties of the stellar parameters are assumed to be the quadratic sum of the quoted internal uncertainties and the external uncertainties calculated from

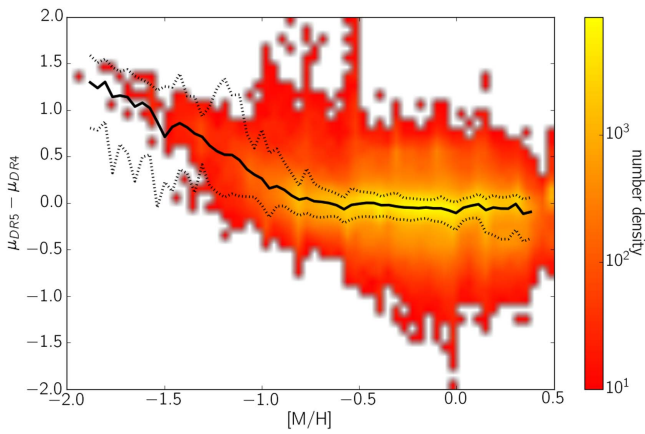


Figure 23. Difference between the derived distance modulus found in DR5 and that found in DR4, as a function of DR5 [M/H]. While there is some scatter at all metallicities, the clearest trend is toward greater distances in DR5 at [M/H] $\lesssim -1$. This is due to the absence of isochrones with [M/H] < -0.9 in the set used to derive distances for DR4. The solid black line indicates the median in bins of 0.03 dex in [M/H], and the dotted lines indicate the 1 σ equivalent range.

stars with S/N > 40 (Table 4). $P(\text{model})$ is our prior and $P(\text{data})$ is a normalization that we can safely ignore.

The method we use to derive the distances for DR5 is nearly the same as that used by DR4, and we refer readers to Binney et al. (2014) for details. We apply the same priors on stellar location, age, metallicity, and initial mass, and on the line-of-sight extinction to the stars. These are all described in Section 2 of Binney et al. (2014). The isochrone set that we use has been updated to the PARSEC v1.1 set (Bressan et al. 2012), which provide values for 2MASS J , H , and K_s magnitudes, so we no longer need to obtain 2MASS magnitudes by transforming Johnston–Cousins–Glass magnitudes, as we did when calculating the distances for DR4. Whereas the isochrones used by Binney et al. (2014) went no lower in metallicity than $Z = 0.00220$ ([M/H] = -0.914), the new isochrones extend to $Z = 0.00010$ ([M/H] = -2.207)—see Table 6. The new isochrones have a clear impact on distances to stars at lower metallicities (Figure 23). Experiments on a subset of stars using isochrones more closely spaced in Z found that the inclusion of more isochrones has negligible impact on the derived properties of the stars.

The distance pipeline determines a full pdf, $P(\text{model}|\text{data})$, for all the parameters used to describe the stars and their positions. We characterize this pdf in terms of expectation values and formal uncertainties for [M/H], $\log_{10}(\tau)$, initial mass, and $\log_{10}(A_V)$ (marginalizing over all other properties). For the distance we provide several characterizations of the pdf: expectation values and formal uncertainties for the distance itself (s), for the distance modulus (μ), and for the parallax ϖ . As pointed out by Binney et al. (2014), it is inevitable that the expectation values (denoted as e.g., $\langle s \rangle$) are such that $\langle s \rangle > s_{(\mu)} > 1/\langle \varpi \rangle$ (where $\log_{10}s_{(\mu)} = 1 + \langle \mu \rangle/5$ and s is in parsecs). In addition we provide multi-Gaussian fits to the pdfs in distance modulus.

As shown in Binney et al. (2014), the pdfs in distance are not always well represented by an expectation value and uncertainty (which are conventionally interpreted as the mean and dispersion of a Gaussian distribution). A number of the pdfs are double- or even triple-peaked (typically because it cannot be definitively determined whether the star is a dwarf or

a giant), and approximating this as a single Gaussian is extremely misleading. The multi-Gaussian fits to the pdfs in μ provide a compact representation of the pdf, and can be written as

$$P(\mu) = \sum_{k=1}^N \frac{f_k}{\sqrt{2\pi}\sigma_k} \exp\left(-\frac{(\mu - \mu_k)^2}{2\sigma_k^2}\right), \quad (5)$$

where the number of components N , the means μ_k , weights f_k , and dispersions σ_k are determined by the pipeline. DR5 gives these values as *number_of_Gaussians_fit* (for N), and for $k = 1, 2, 3$ as *mean_k*, *sig_k*, and *frac_k* (corresponding to μ_k , σ_k , and f_k respectively).

To determine whether a distance pdf is well represented by a given multi-Gaussian representation in μ we take bins in distance modulus of width $w_i = 0.2$, which contain a fraction p_i of the total probability taken from the computed pdf and a fraction P_i from the Gaussian representation, and compute the goodness-of-fit statistic

$$F = \sum_i \left(\frac{p_i}{w_i} - \frac{P_i}{w_i} \right)^2 \tilde{\sigma} w_i, \quad (6)$$

where the weighted dispersion

$$\tilde{\sigma}^2 \equiv \sum_{k=1,N} f_k \sigma_k^2$$

is a measure of the overall width of the pdf. Our strategy is to represent the pdf with as few Gaussian components as possible, but if the value of F is greater than a threshold value ($F_t = 0.04$), or the dispersion associated with the model differs by more than 20% from that of the complete pdf, then we conclude that the representation is inadequate, and add another Gaussian component to the representation (to a maximum of three components). For around 45% of the stars, a single Gaussian component proves adequate, while around 51% are fitted with two Gaussians, and only 4% require a third component. The value of F is provided in the database as *CHISQ_Binney* and we also include a flag (denoted *FitFLAG_Binney*) that is nonzero if the dispersion of the fitted model differs by more than 20% from that of the computed pdf. Typically the problems flagged are rather minor (as shown in Figure 3 of Binney et al. 2014).

Using the derived distance moduli and extinctions, it is simple to plot an absolute color–magnitude diagram, from which we can check that the pipeline produces broadly sensible results. It was inspection of this plot that led us to filter out dwarfs with $T_{\text{eff}} \leq 4000$ K and hot, metal-poor stars, because they fell in implausible regions of the diagram. We show this plot, constructed from the filtered data, in Figure 24.

To test the output from the pipeline, we compare the derived parallaxes (and uncertainties) with those found by *Hipparcos* (van Leeuwen 2007) for the ~ 5000 stars common to the two catalogs. It is important to compare parallax with parallax, because, as noted before, $\langle \varpi \rangle > 1/\langle s \rangle$, so this is the only fair test. We therefore consider the statistic Δ , which we define as

$$\Delta = \frac{\langle \varpi_{\text{DR5}} \rangle - \overline{\varpi}_{\text{H}}}{\sqrt{\sigma_{\varpi, \text{DR5}}^2 + \sigma_{\varpi, \text{H}}^2}}, \quad (7)$$

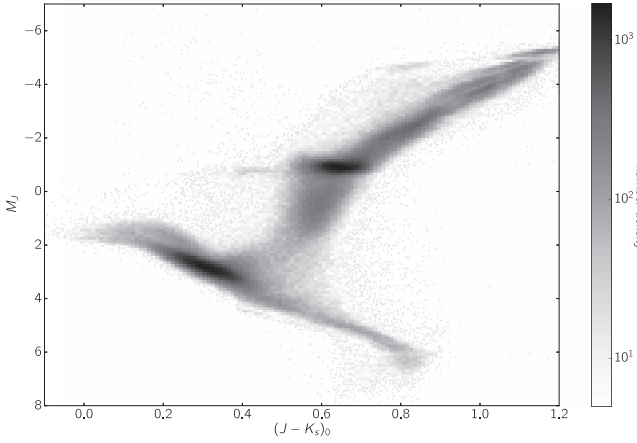


Figure 24. Absolute color–magnitude diagram, derived from the pipeline outputs, for all stars in the filtered distance catalog. The values are found from the values in the catalog as $M_J = J - \langle \mu \rangle - 0.282 \times \tilde{A}_V$ and $(J - K_s)_{\text{abs}} = J - K_s - 0.17 \times \tilde{A}_V$ where $\log_{10} \tilde{A}_V = \langle \log_{10} A_V \rangle$. Shading indicates the number of stars in bins of width 0.01 mag in $(J - K_s)_0$ and 0.1 mag in M_J . If there are fewer than five stars in a bin, they are represented as points.

where ϖ_H is the quoted *Hipparcos* parallax and $\sigma_{\varpi, H}$ the quoted uncertainty, while ϖ_{DR5} and $\sigma_{\varpi, \text{DR5}}$ are the same quantities from the distance pipeline. Ideally, Δ would have a mean value of zero and a dispersion of unity.

In Figure 25 we plot a histogram of the values of Δ for these stars separated into giants ($\log g \leq 3.5$), cool dwarfs ($\log g > 3.5$ and $T_{\text{eff}} \leq 5500$ K), and hot dwarfs ($\log g > 3.5$ and $T_{\text{eff}} > 5500$ K), as well as for the subset of giants that we associate with the red clump ($1.7 < \log g < 2.4$ and $0.55 < J - K_s < 0.8$). We have “sigma clipped” the values, such that none of the (very few) stars with $|\Delta| > 4$ contributes to the statistics. The results are all pleasingly close to having zero mean and a dispersion of unity, especially the giants. We tend to slightly overestimate the parallaxes of the hot dwarfs, and slightly underestimate those of the cool dwarfs (corresponding to *underestimated* distances to the hot dwarfs and *overestimated* distances to the cool dwarfs). This represents an improvement over the comparable figures for DR4, except for a very slightly worse mean value for the cool dwarfs (and even for these stars, there is an improvement in that the dispersion is now closer to unity).

With the release of the TGAS data it becomes possible to construct a figure such as Figure 25 using the majority of RAVE stars. Thus much more rigorous checks of our distance (parallax) estimates are now possible. When that has been done and systematics calibrated out, we will be able to provide distances to all stars that are more accurate than those based on either DR5 or TGAS alone, by feeding the TGAS data, including parallaxes, into the distance pipeline.

Where stars have been observed more than once by RAVE, we recommended using the distance (and other properties) obtained from the spectrum with the highest signal-to-noise ratio. However, DR5 reports distances from each spectrum.

10. IRFM TEMPERATURES

The IRFM (Blackwell & Shallis 1977; Blackwell et al. 1979) is one of the most accurate techniques for deriving stellar effective temperatures in an almost model-independent way. The basic idea is to measure for each star its bolometric flux and a

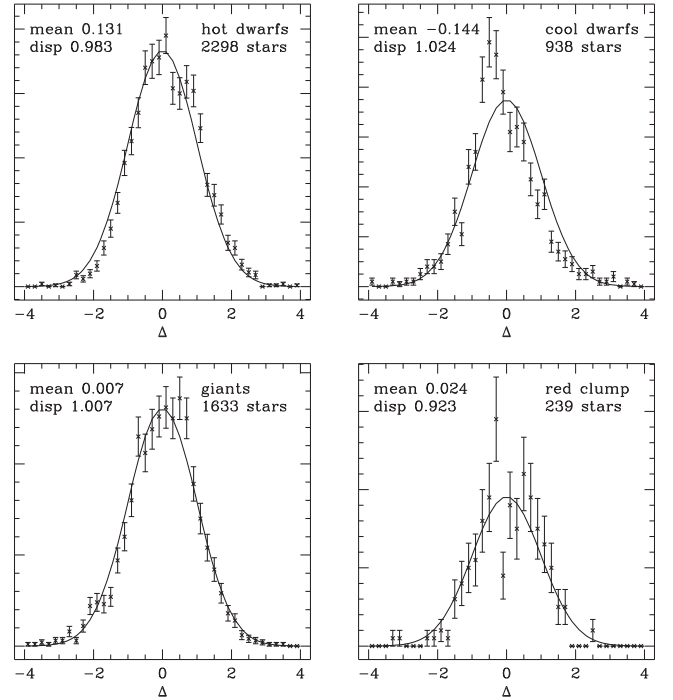


Figure 25. Comparison of the parallax estimates found by the DR5 pipeline and those found by *Hipparcos*. The statistic Δ is defined in Equation (7), and ideally has a mean of zero and dispersion of unity. The points are a histogram of Δ , with error bars given by the expected \sqrt{N} Poisson noise in each bin. The solid line is a Gaussian with the desired mean and dispersion. Stars are divided into “hot dwarfs” ($T_{\text{eff}} > 5500$ K and $\log g > 3.5$), “cool dwarfs” ($T_{\text{eff}} < 5500$ K and $\log g > 3.5$), and “giants” ($\log g < 3.5$), as labeled. The “red clump” stars are a subset of the giants, with $1.7 < \log g < 2.4$ and $0.55 < J - K_s < 0.8$.

monochromatic infrared flux. Their ratio is then compared to that obtained for a surface at T_{eff} , i.e., σT_{eff}^4 divided by the theoretical monochromatic flux. The latter quantity is relatively easy to predict for spectral types earlier than $\sim M0$, because the near-infrared region is dominated by the continuum, and the monochromatic flux is proportional to T_{eff} (Rayleigh–Jeans regime), so dependences on other stellar parameters (such as $[\text{Fe}/\text{H}]$ and $\log g$) and model atmospheres are minimized (as extensively tested in the literature, e.g., Alonso et al. 1996; Casagrande et al. 2006). The method thus ultimately depends on a proper derivation of stellar fluxes, from which T_{eff} can then be derived. Here we adopt an updated version of the IRFM implementation described in Casagrande et al. (2006, 2010), which has been validated against interferometric angular diameters (Casagrande et al. 2014) and combines APASS $BVg'r'i'$ together with 2MASS JHK_s to recover the bolometric and infrared flux of each star. The flux outside photometric bands (i.e. the bolometric correction) is derived using a theoretical model flux at given T_{eff} , $[\text{Fe}/\text{H}]$, and $\log g$. An iterative procedure in T_{eff} is adopted to cope with the mildly model-dependent nature of the bolometric correction and of the theoretical surface infrared monochromatic flux. For each star, we interpolate over a grid of synthetic model fluxes, starting with an initial estimate of the stellar effective temperature and fixing $[\text{Fe}/\text{H}]$ and $\log g$ to the RAVE values, until convergence is reached within 1 K in effective temperature.

In a photometric method such as the IRFM, reddening can have a non-negligible impact and must be corrected for. For each target RAVE provides an estimate of $E(B - V)$ from Schlegel

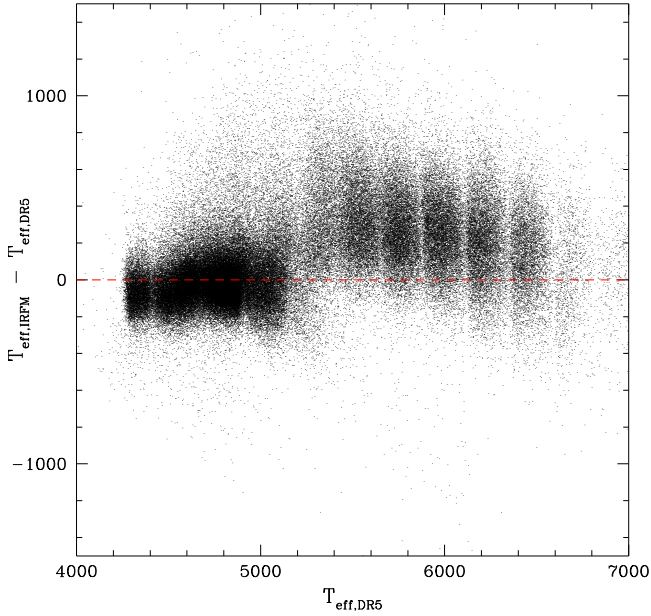


Figure 26. Comparison between the temperatures derived from the IRFM and those in DR5. Only stars with $S/N > 50$ and $\text{AlgoConv} = 0$ are shown. The giants, with $T_{\text{eff}} < 5500$ K, have temperatures that agree well with IRFM temperatures, but there is a systematic offset to the main-sequence/turnoff stars. The pixelization, an artifact of the RAVE stellar parameter pipeline, is apparent as vertical bands.

et al. (1998). These values, however, are integrated over the line of sight, and in the literature there are several indications suggesting that reddening from this map is overestimated, particularly in regions of high extinction (e.g., Arce & Goodman 1999; Schlafly & Finkbeiner 2011). To mitigate this effect, we recalibrate the map of Schlegel et al. (1998) using the intrinsic color of clump stars, identified as number overdensities in color distribution (and thus independently of the RAVE spectroscopic parameters). We take the 2MASS stellar catalog, tessellate the sky with boxes of $10^\circ \times 10^\circ$, and select stars in the magnitude range of RAVE. Within each box we can easily identify the overdensity due to clump stars, whose position in $J - K_s$ color is little affected by their age and metallicity. Thus, despite the presence of metallicity and age gradients across the Galaxy (e.g., Boeche et al. 2014; Casagrande et al. 2016), we can regard the average $J - K_s$ color of clump stars as a standard crayon. We take the sample of clump stars from Casagrande et al. (2014), for which reddening is well constrained, and use their median unreddened $(J - K_s)_0$ against the median measured at each n -tessellation, to derive a value of reddening at each location $E(J - K)_n = (J - K_s)_n - (J - K_s)_0$. We then compare these values of reddening with the median ones obtained using the map of Schlegel et al. (1998) over the same tessellation. The difference between the reddening values we infer and those from the map is well fitted as function of $\log(b)$ up to $\approx 40^\circ$ from the Galactic plane. We use this fit to rescale the $E(B - V)$ from the map of Schlegel et al. (1998), thus correcting for its tendency to overestimate reddening, while at the same time keeping its superior spatial resolution (\sim arcmin). For $|b| \gtrsim 40^\circ$ the extinction is low and well described.

Figure 26 shows a comparison between the DR5 temperatures and those from the IRFM, $T_{\text{eff,IRFM}}$. Stars with temperatures cooler than $T_{\text{eff}} \sim 5300$ K show a good agreement between $T_{\text{eff,IRFM}}$ and $T_{\text{eff,DR5}}$, with a scatter of

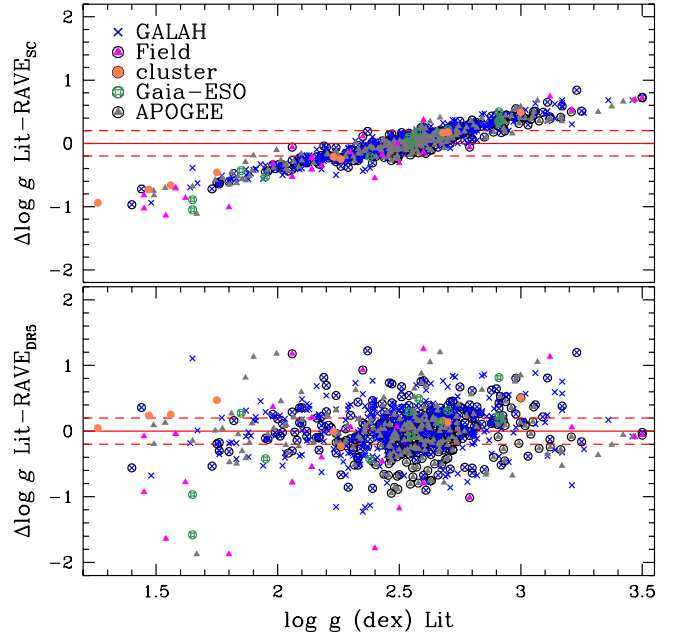


Figure 27. Top: the difference between the asteroseismically calibrated gravity, $\log g_{\text{sc}}$, and that from various sources in the literature as a function of literature $\log g$. Only stars with $S/N > 40$, $\text{Flag}_M = 1$, and $\text{AlgoConv} = 0$ are shown. The black open circles designate those stars with $\text{Flag}_{050} = 1$, which in general are the stars at the extremes of the calibration. Bottom: the same stars as in the top panel, but the gravities in the main DR5 catalog are used.

~ 150 K, which is the typical uncertainty of the RAVE temperatures. Stars hotter than $T_{\text{eff}} = 5300$ K have an offset in temperature, in the sense that $T_{\text{eff,IRFM}}$ is approximately 350 K warmer than $T_{\text{eff,DR5}}$ at 5500 K. As the temperature increases, the temperature offset decreases to ~ 100 K at 7000 K. This offset is consistent with what is seen in a comparison between RAVE and other data sets (see, e.g., Table 4 and Figures 14 and 18), thus suggesting that the offset is unlikely to stem from the IRFM only. From Table 4 it is evident that the IRFM temperatures for especially the cool dwarfs are in better agreement with high-resolution studies than the spectroscopic DR5 temperatures.

Nevertheless, we remark that various reasons might be responsible for this trend: first, the rescaling of the map of Schlegel et al. (1998) is based on clump stars, so it is not surprising that best agreement is found for giant stars. Turnoff and main-sequence stars are on average closer than intrinsically brighter giants, so despite the rescaling, $E(B - V)$ will on average still be overestimated, implying higher effective temperatures in the IRFM. Also, at the hottest T_{eff} the contribution of optical photometry becomes increasingly important, as do proper control over the standardization, and absolute calibration of the APASS photometry.

11. ASTEROSEISMICALLY CALIBRATED RED GIANT CATALOG

Asteroseismic data provide a very accurate way to determine surface gravities of red giant stars (e.g., Stello et al. 2008; Mosser et al. 2010; Bedding et al. 2011). When solar-like pulsations in red giants can be detected, the pulsation frequencies, such as the average large frequency separation, $\langle \Delta\nu \rangle$, and the frequency of maximum oscillation power, ν_{max} ,

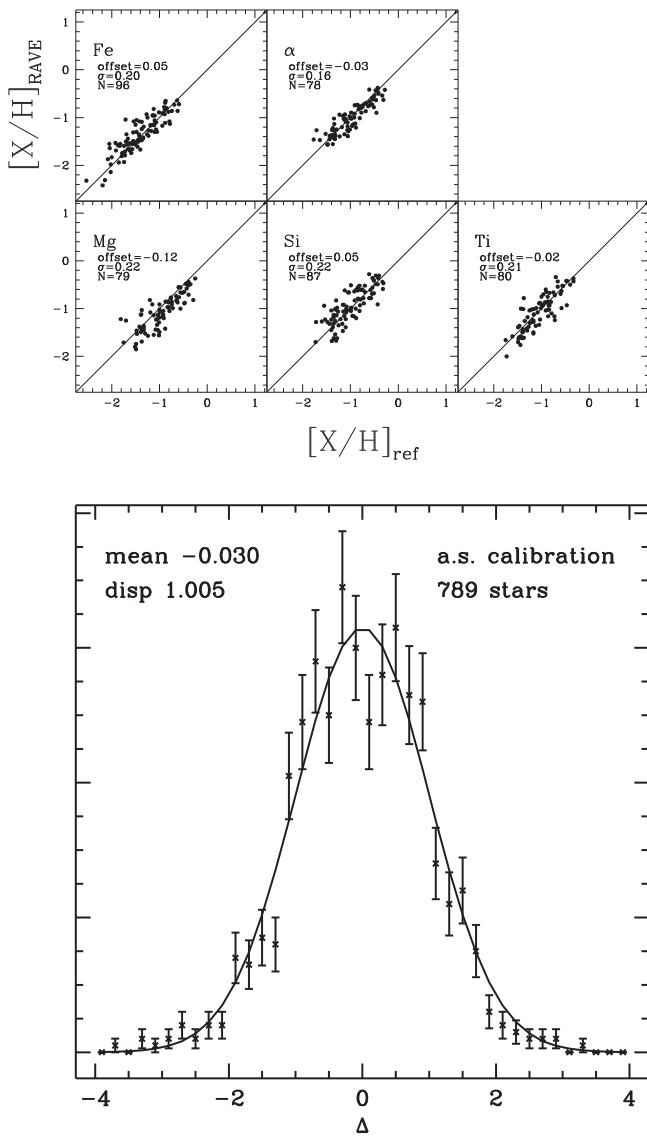


Figure 28. Comparison of the elemental abundances from the RAVE chemical pipeline (top) and parallax estimates found from the DR5 distance pipeline but using $\log g_{\text{sc}}$ and IRFM temperatures as an input. Only stars with $\text{Flag_M} = 1$ are considered.

can be used to obtain the density and surface gravity of the star. Exquisite data sets with which to search for oscillations have arisen in the space-based missions *CoRoT* and *Kepler*, and it has already been shown that their long data set in time gives the frequency resolution needed to extract accurate estimates of the basic parameters of individual modes covering several radial orders, such as frequencies, frequency splittings, amplitudes, and damping rates.

Pulsations in red giants have significantly longer periods and larger amplitudes than in solar-type stars, so oscillations may be detected in fainter (more numerous) targets observed with long cadence. Further, the seismic $\log g$ values are almost fully independent of the input physics in the stellar evolution models that are used (e.g., Gai et al. 2011). This makes the use of red giants with asteroseismic $\log g$ values ideal to check and calibrate surface gravities that are obtained spectroscopically.

V17 present 72 RAVE stars with solar-like oscillations detected by the *K2* mission. The finite length and cadence of the observations of a *K2* field means there is a limit to our ability to

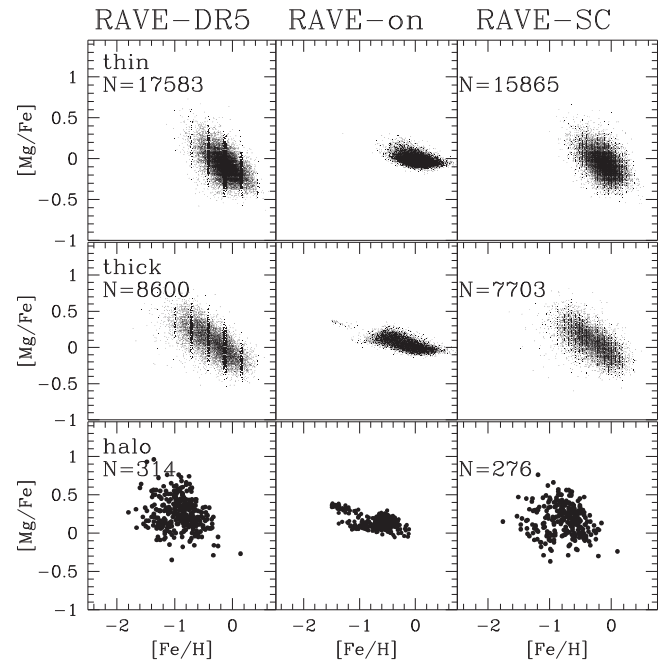


Figure 29. Abundance ratio $[Mg/Fe]$ vs. the metallicity $[Fe/H]$ for the thin-disk component (top), the thick-disk component (middle panel), and the halo component (bottom panel) for parameters from RAVE-on, RAVE DR5, and the seismically calibrated RAVE stars.

extract properties from solar-like oscillations, and hence for how well $\langle \Delta \nu \rangle$ and ν_{max} can be obtained (e.g., Davies & Miglio 2016). This means that the asteroseismic calibration based on the *K2* stars is limited to roughly the range of $2.1 < \log g < 3.35$ dex. For the color interval $0.50 < J - K_s < 0.85$, which was shown to be appropriate for selecting red giant stars in the *Kepler* field, the spectroscopic gravities present in the RAVE catalog are calibrated against the seismic gravities. This calibration is a function only of RAVE $\log g_p$ and does not depend on photometric color, metallicity, or S/N. Whereas the reddening maps of Schlegel et al. (1998) indicate that the $(J - K)$ reddening in the *K2* field is negligible, RAVE observes many reddened stars. Therefore, the dereddened color range is kept unchanged, and DR5 includes $\log g$ calibrated according to V17 only when the dereddened color $(J - K_s)_0$ lies in the interval (0.50, 0.85).

There are 207,050 RAVE stars that fall within $0.50 < (J - K_s)_0 < 0.85$; 200,524 of these have a RAVE $\log g$, enabling the application of an asteroseismic calibration. Because of the RAVE $\log g$ uncertainties, misclassifications of red giants can occur, i.e., red giants can have gravities that indicate they are dwarfs or supergiant stars. Therefore each asteroseismically calibrated RAVE star has a flag, Flag050 , indicating whether the seismically calibrated $\log g$, $\log g_{\text{sc}}$, and the DR5 $\log g_p$ are within 0.5 dex of each other. The flag Flag_M specifies whether all 20 classification flags of Matijević et al. (2012) point to the star being “normal”, which likely means the star is indeed a typical red giant. Therefore, stars with both $\text{Flag050} = 1$ and $\text{Flag_M} = 1$ point to an especially desirable sample of asteroseismically calibrated giants.

Figure 27 shows $\log g_{\text{sc}}$ compared to the gravities from the RAVE stars observed by the APOGEE, GALAH, and *Gaia*-ESO surveys, as well as the RAVE cluster and external stars (from Section 7). The scatter about these 906 stars with

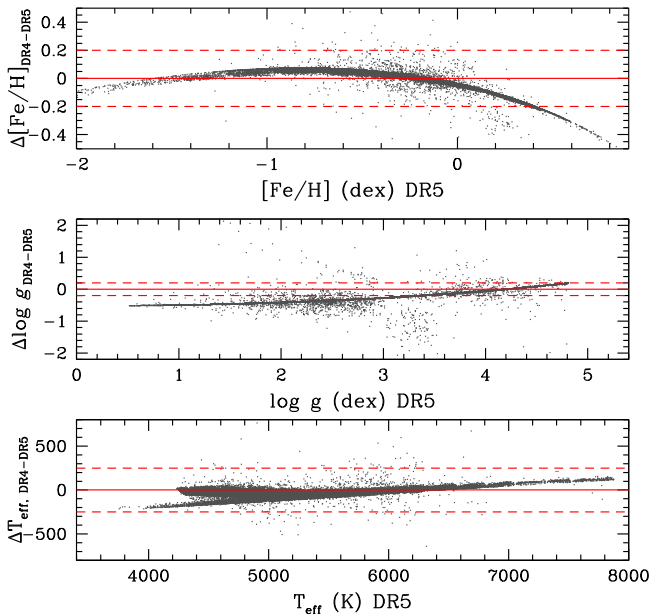


Figure 30. Difference in the stellar parameters T_{eff} (bottom), $\log g$ (middle), and $[M/H]$ (top) between RAVE DR4 and DR5. Only stars with $S/N > 40$ and $\text{AlgoConv} = 0$ are shown.

$S/N > 40$, $\text{Flag}_M = 1$, and $\text{AlgoConv} = 0$ is $\sigma \log g_{\text{sc}} = 0.35$ dex. This is a 12% smaller scatter than when using the RAVE DR5 $\log g$ from the main catalog. When additionally imposing the criterion $\text{Flag}_{050} = 1$, $\sigma \log g_{\text{sc}} = 0.26$ dex, which is a 25% smaller scatter than when using the RAVE DR5 $\log g$. Tables 4 and 5 summarize how $\log g_{\text{sc}}$ compares with external results. The criterion $\text{Flag}_M = 1$ is implemented in these comparisons.

Combining the $\log g_{\text{sc}}$ with the temperatures from the IRFM, the RAVE chemistry (Section 8) and distance pipeline (Section 9) are rerun. Neither the uncertainty in chemical pipeline nor the uncertainty in distance changes when using the more accurate $\log g_{\text{sc}}$ and IRFM temperatures as an input, as seen in Figure 28. The seismically calibrated giants are presented in a separate table, along with the elemental abundances and distances derived.

12. USE OF DIFFERENT RAVE STELLAR PARAMETERS

12.1. DR5 Main Catalog versus RAVE-on

While our official DR parameters are constantly under improvement, other approaches to determining parameters from RAVE spectra have become public. One example is the result from C16, who present the RAVE-on catalog by the data-driven approach *The Cannon*. In short, this method is based on training the data on a set for which more information is known by independent means (i.e., spectra of the stars in other wavelength domains, asteroseismic observations, etc.). The disadvantage, however, is that the performance of the results relies fully on the training set. For example, as seen in C16, if the training set does not contain metal-poor stars, the derived metallicities from survey stars will lack a metal-poor population as well. The RAVE training sample used in C16 was inhomogeneous, using RAVE overlap stars from APOGEE, Fulbright et al. (2010), and Ruchti et al. (2011) for the giants, and RAVE overlap stars from LAMOST and the fourth RAVE

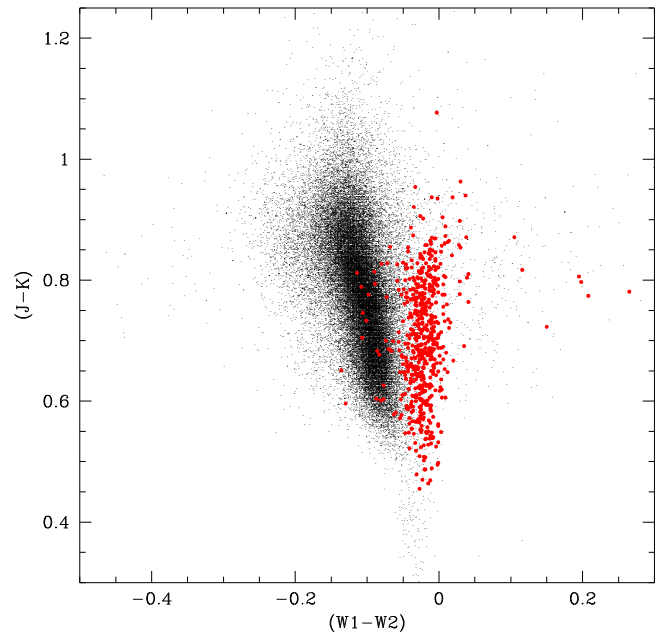


Figure 31. Color-color diagram of the RAVE giants, with the most metal-poor RAVE stars overplotted in red. RAVE can be used to refine criteria and quantify likelihood to photometrically select metal-poor stars for spectroscopic follow-up.

data release for the main-sequence stars. Unlike for the giants, the training sample for the main-sequence stars did not have known elemental abundances, so no elemental abundances could be derived for main-sequence stars.

The main RAVE DR5 catalog, on the other hand, is based on stellar physics—the use of a grid of synthetic spectra over a large parameter space is utilized to derive stellar parameters. Therefore for each star there is a physical justification ensuring the coherence of the obtained stellar parameters. This leads to cases in which no feasible match to a theoretical spectrum can be made, and so unlike in *The Cannon*, there are instances in which the algorithm does not converge. Also, stellar parameters are obtained along the gridlines of the synthetic spectra, leading to pixelization of the values, different visually to the smooth interpolation of *The Cannon*.

Figure 29 shows the metallicities and Mg elemental abundances of thin-disk, thick-disk, and halo RAVE stars for the RAVE DR5 and RAVE-on stars. The maximum distance above the plane (z_{max}), rotational velocity, and eccentricity were used to separate these components as described by Boeche et al. (2013). These parameters were computed by integrating the orbits of the RAVE stars using *galpy* (Bovy 2015), where the input parameters were the radial velocities and distances presented here, as well as the TGAS proper motions. We opted to not use the TGAS parallaxes to determine distances, because this is nontrivial (Bailer-Jones 2015; Astraatmadja & Bailer-Jones 2016).

Figure 29 illustrates the narrower chemical sequences of RAVE-on, due in part to smaller formal uncertainties in $[\text{Mg}/\text{Fe}]$ and $[\text{Fe}/\text{H}]$, and the smooth interpolation of the stellar parameters (i.e., no pixelization). It can also be seen that RAVE DR5 has a larger sample of stars with elemental abundances, and a more physical distribution for stars with $[\text{Fe}/\text{H}] < -1$ dex. This is due to the difficulty of obtaining main-sequence stars needed to train *The Cannon* (C16).

Table 4 quantifies the agreement from external stars of the T_{eff} , $\log g$, and $[\text{Fe}/\text{H}]$ presented in RAVE-on and in RAVE DR5. C16 performed external validation of the RAVE-on stellar parameters on cool stars (F, G, and K stars), and here we extend this. There is no significant difference in the precision when comparing the RAVE-on and RAVE DR5 stellar parameters to those from high-resolution stars. RAVE-on lacks metal-poor stars in the training sample, leading to a worse agreement for stars with $[\text{Fe}/\text{H}]$ metallicities more metal-poor than -1 dex. It also is on a different metallicity scale than RAVE DR5, on average 0.15 dex more metal-poor than RAVE DR5. There are more RAVE stars with derived stellar parameters— T_{eff} , $\log g$, and $[\text{Fe}/\text{H}]$ —in RAVE-on, and more stars with elemental abundances in RAVE DR5.

12.2. DR5 Main Catalog T_{eff} versus IRFM T_{eff}

The IRFM temperatures and those from the main DR5 are similar, as shown in Figure 26, and as discussed in Section 10. However, there is better agreement between RAVE stars observed from high-resolution studies and $T_{\text{eff,IRFM}}$ (see Table 4). Moreover, $T_{\text{eff,IRFM}}$ is available for 95% of the RAVE stars, and is independent of S/N. Temperatures from the IRFM are critical for the RAVE stars that were released in DR1, because during the first year of RAVE operations, no blocking filter was used to isolate the spectral range required, and as a result, the spectra collected were contaminated by the second order. Hence, although the determination of radial velocities is still straightforward, stellar parameters cannot be reliably determined from the spectra. IRFM temperatures are further especially valuable for stars with temperatures lower than 4000 K and for stars hotter than 8000 K, because the main DR5 catalog is only able to determine temperatures for stars in the range 4000–8000 K.

12.3. DR5 Main Catalog $\log g$ versus $\log g_{\text{sc}}$

A direct asteroseismic calibration can be carried out for RAVE stars with colors in the range $0.50 < (J - K_s)_0 < 0.85$, as described by V17. This calibration uses the raw DR5 $\log g$ as a starting point, and therefore any problems in the derivation of the raw DR5 $\log g$ are also carried over to $\log g_{\text{sc}}$. Figure 27 shows how $\log g_{\text{sc}}$ compares to $\log g_{\text{DR5}}$ for external stars observed with high resolution. $\log g_{\text{sc}}$ agrees with external estimates $\sim 12\%$ better than $\log g_{\text{DR5}}$. However, we note the linear relation between $\log g_{\text{sc}}$ and gravities from the literature, suggesting that minor biases are present in $\log g_{\text{sc}}$, in a sense that $\log g$ values less than 2.3 dex are underestimated and $\log g$ values greater than 2.8 dex are overestimated. This can be minimized by selecting stars with $\text{Flag050} = 1$. There is no correlation between literature $\log g$ and $\log g_{\text{DR5}}$.

13. DIFFERENCES BETWEEN DR4 AND DR5

RAVE DR5 differs from DR4 in a number of ways, as listed below.

1. The DR5 RAVE sample is larger than DR4 by $\sim 30,000$ stars. This is due in part to the inclusion of the 2013 data, but mainly to the improvement of the DR5 reduction pipeline, which now processes data on a fiber-by-fiber basis instead of a field-by-field basis.

2. The DR1 data are now ready to be ingested through the same reduction pipeline, improving the homogeneity of the DR5 radial velocities compared to those in DR4.
3. The error spectra now available for all RAVE stars have yielded more accurate uncertainties on the RAVE radial velocities and stellar parameters, especially for low-S/N and hot stars. We plan to extend the analysis of error spectra to the chemical elements in a future release.
4. A new calibration of T_{eff} , $\log g$, and $[\text{M}/\text{H}]$ has been applied, increasing the accuracy of the stellar parameters by up to 15%. This calibration is employed mainly because there are now RAVE stars with $\log g$ values determined asteroseismically (V17). The metal-rich tail of the RAVE stars has also been re-investigated, by increasing the number of calibration stars in the super-solar metallicity regime. Hence the updated DR5 stellar parameters mainly improve the gravities of the giants and the supersolar $[\text{M}/\text{H}]$ stars. Figure 30 shows how the atmospheric parameters in DR5 differ from those in DR4.
5. A sample of RAVE giants is provided for which the V16 asteroseismic calibration can be applied. These $\log g$ parameters are the most accurate, but can only be applied to stars that fall within $0.50 < (J - K_s)_0 < 0.85$.
6. Although the chemical pipeline is the same as the one employed in DR4, the stellar parameters fed into this pipeline are better calibrated, and hence the resulting elemental abundances are slightly changed. The $[\text{Fe}/\text{H}]$ and $[\text{X}/\text{Fe}]$ abundances are shifted by ~ 0.1 dex to be more metal-rich than in DR4.
7. The distance pipeline has been improved, especially for the metal-poor stars. In DR5, we list individual distances per spectrum and not per star; for stars that have been observed more than once (indicated by the `Rep_Flag`), we recommend use of the distance from the spectrum with the highest S/N.
8. For the first time, photometry from APASS and *WISE* can be matched with RAVE stars. This development opens new ways to do science with the database. For example, Figure 31 shows the RAVE giants in a 2MASS–*WISE* color–color plot. The most metal-poor giants observed by RAVE ($[\text{Fe}/\text{H}] < -2$ dex) are overplotted in red. These metal-poor stars have been identified by projecting all RAVE spectra on a low-dimensional manifold using the t-Distributed Stochastic Neighbor Embedding (t-SNE) and then reanalyzing the metallicity, via the CaT lines, of all RAVE stars in the manifold that is mostly populated by very metal-poor stars (G. Matijević et al. 2017, in preparation). It is evident that they occupy a distinct *WISE* color range. The comprehensive RAVE data set may be used as a test bed to define cuts in color space to select metal-poor candidates, which can then be applied to fainter samples than RAVE probed or to regions RAVE has not surveyed (e.g., Schlafman & Casey 2014).
9. The inclusion of APASS photometry also allows for the determination of IRFM temperatures, which are provided for more than 95% of the RAVE sample.

14. CONCLUSIONS

The RAVE DR5 presents radial velocities for 457,589 individual stars in the brightness range $9 < I < 12$ mag,

Table 7
Main DR5 Catalog Description

Col.	Format	Units	NULL	Label	Explanations
1	char	...	N	RAVE_OBS_ID	Target designation
2	char	...	N	HEALPix	Hierarchical Equal-Area iso-Latitude Pixelisation value (Note 1)
3	char	...	N	RAVEID	RAVE target designation
4	double	deg	N	RAdeg	Right ascension
5	double	deg	N	DEdeg	Declination
6	double	deg	N	Glon	Galactic longitude
7	double	deg	N	Glat	Galactic latitude
8	float	km s ⁻¹	N	HRV	Heliocentric radial velocity
9	float	km s ⁻¹	N	eHRV	HRV error
10	float	km s ⁻¹	N	StdDev_HRV	Standard deviation in HRV from 10 resampled spectra
11	float	km s ⁻¹	N	MAD_HRV	Median absolute deviation in HRV from 10 resampled spectra
12	float		Y	STN_SPARV	Signal-to-noise ratio calculated by SPARV (Note 2)
13	float	...	Y	S/N_K	Signal-to-noise value (Note 2)
14	float	K	Y	Teff_K	Effective temperature (Note 2)
15	float	K	Y	Teff_N_K	Calibrated effective temperature (Note 2)
16	float	K	Y	eTeff_K	Error effective temperature (Note 2)
17	float	K	N	MAD_Teff_K	Median absolute deviation in Teff_K from 10 resampled spectra
18	float	K	N	StdDev_Teff_K	Standard deviation in Teff_K from 10 resampled spectra
19	float	dex	Y	logg_K	Log gravity (Note 2)
20	float	dex	Y	logg_N_K	Calibrated log gravity (Note 2)
21	float	dex	Y	elogg_K	Error log gravity (Note 2)
22	float	dex	N	MAD_logg_K	Median absolute deviation in logg_K from 10 resampled spectra
23	float	dex	N	StdDev_logg_K	Standard deviation in logg_K from 10 resampled spectra
24	float	dex	Y	Met_K	Metallicity [M/H] (Note 2)
25	float	dex	Y	Met_N_K	Calibrated metallicity [M/H] (Note 2)
26	float	dex	Y	eMet_K	Error metallicity [M/H] (Note 2)
27	float	dex	N	MAD_Met_K	Median absolute deviation in Met_K from 10 resampled spectra
28	float	dex	N	StdDev_Met_K	Standard deviation in Met_K from 10 resampled spectra
29	float	...	Y	CHISQ_K	χ^2 of the stellar parameter pipeline (Note 2)
30	float	...	Y	Algo_Conv_K	Quality flag for stellar parameter pipeline [0...4] (Note 2, Note 4)
31	float	K	Y	Teff_IR	Temperature from infrared flux method
32	float	K	Y	eTeff_IR	Internal error on Teff_IR
33	char	...	N	IR_direct	infrared flux method flag (Note 5)
34	float	dex	Y	Mg	Abundance of Mg [Mg/H]
35	int	...	Y	Mg_N	Number of spectral lines used for calculation of abundance
36	float	dex	Y	Al	Abundance of Al [Al/H]
37	int	...	Y	Al_N	Number of spectral lines used for calculation of abundance
38	float	dex	Y	Si	Abundance of Si [Si/H]
39	int	...	Y	Si_N	Number of spectral lines used for calculation of abundance
40	float	dex	Y	Ti	Abundance of Ti [Ti/H]
41	int	...	Y	Ti_N	Number of spectral lines used for calculation of abundance
42	float	dex	Y	Fe	Abundance of Fe [Fe/H]
43	int	...	Y	Fe_N	Number of spectral lines used for calculation of abundance
44	float	dex	Y	Ni	Abundance of Ni [Ni/H]
45	int	...	Y	Ni_N	Number of spectral lines used for calculation of abundance
46	float	dex	Y	Alpha_c	Alpha-enhancement from chemical pipeline (Note 2)
47	float	...	Y	CHISQ_c	χ^2 of the chemical pipeline (Note 2)
48	float	...	Y	frac_c	Fraction of spectrum used for calculation of abundances (Note 2)
49	float	mag	Y	AV_Schlegel	Total extinction in V-band from Schlegel et al. (1998)
50	float	kpc	Y	distance	Spectrophotometric distance (Binney et al. 2014)
51	float	kpc	Y	edistance	Error on distance (Binney et al. 2014)
52	float	mag	Y	log_Av	Log Av extinction (Binney et al. 2014)
53	float	mag	Y	eelog_Av	Error on log_Av (Binney et al. 2014)
54	float	mas	Y	parallax	Spectrophotometric parallax (Binney et al. 2014)
55	float	mas	Y	eparallax	Error on parallax (Binney et al. 2014)
56	float	mag	Y	DistanceModulus_Binney	Distance modulus (Binney et al. 2014)
57	float	mag	Y	eDistanceModulus_Binney	Distance modulus (Binney et al. 2014)
58	int	...	Y	Fit_Flag_Binney	See final paragraph Section 3 of Binney et al. (2014)
59	float	...	Y	FitQuality_Binney	Given by symbol "F" in Equation (15) of Binney et al. (2014)
60	int	...	Y	N_Gauss_fit	Number of components required for multi-Gaussian distance modulus fit
61	int	...	Y	Gauss_mean_1	Property of multi-Gaussian distance modulus fit, see Section 9, Equation (5)
62	float	...	Y	Gauss_sigma_1	Property of multi-Gaussian distance modulus fit, see Section 9, Equation (5)
63	float	...	Y	Gauss_frac_1	Property of multi-Gaussian distance modulus fit, see Section 9, Equation (5)

Table 7
(Continued)

Col.	Format	Units	NULL	Label	Explanations
64	float	...	Y	Gauss_mean_2	Property of multi-Gaussian distance modulus fit, see Section 9, Equation (5)
65	float	...	Y	Gauss_sigma_2	Property of multi-Gaussian distance modulus fit, see Section 9, Equation (5)
66	float	...	Y	Gauss_frac_2	Property of multi-Gaussian distance modulus fit, see Section 9, Equation (5)
67	float	...	Y	Gauss_mean_3	Property of multi-Gaussian distance modulus fit, see Section 9, Equation (5)
68	float	...	Y	Gauss_sigma_3	Property of multi-Gaussian distance modulus fit, see Section 9, Equation (5)
69	float	...	Y	Gauss_frac_3	Property of multi-Gaussian distance modulus fit, see Section 9, Equation (5)
70	char	...	Y	c1	n.th minimum distance (Note 6)
71	char	...	Y	c2	n.th minimum distance (Note 6)
72	char	...	Y	c3	n.th minimum distance (Note 6)
73	char	...	Y	c4	n.th minimum distance (Note 6)
74	char	...	Y	c5	n.th minimum distance (Note 6)
75	char	...	Y	c6	n.th minimum distance (Note 6)
76	char	...	Y	c7	n.th minimum distance (Note 6)
77	char	...	Y	c8	n.th minimum distance (Note 6)
78	char	...	Y	c9	n.th minimum distance (Note 6)
79	char	...	Y	c10	n.th minimum distance (Note 6)
80	char	...	Y	c11	n.th minimum distance (Note 6)
81	char	...	Y	c12	n.th minimum distance (Note 6)
82	char	...	Y	c13	n.th minimum distance (Note 6)
83	char	...	Y	c14	n.th minimum distance (Note 6)
84	char	...	Y	c15	n.th minimum distance (Note 6)
85	char	...	Y	c16	n.th minimum distance (Note 6)
86	char	...	Y	c17	n.th minimum distance (Note 6)
87	char	...	Y	c18	n.th minimum distance (Note 6)
88	char	...	Y	c19	n.th minimum distance (Note 6)
89	char	...	Y	c20	n.th minimum distance (Note 6)
90	int	-	N	Rep_Flag	0: single observation, 1: more than one observation
91	int	-	N	CluStar_Flag	0: not a targeted observation, 1: targeted observation
92	int	-	N	FootPrint_Flag	0: outside RAVE selection function footprint, 1: inside footprint
93	char	-	Y	ID_TGAS_source	TGAS target designation
94	char	-	Y	MatchFlag_TGAS	Crossmatch quality flag (Note 7)
95	float	deg	Y	RA_TGAS	TGAS right ascension (J2015)
96	float	deg	Y	DE_TGAS	TGAS declination (J2015)
97	float	mas yr ⁻¹	Y	pmRA_TGAS	Proper motion RA from TGAS— $\dot{\alpha} \cos(\delta)$
98	float	mas yr ⁻¹	Y	pmRA_error_TGAS	Standard error of proper motion in RA from TGAS
99	float	mas yr ⁻¹	Y	pmDE_TGAS	Proper motion in DE from TGAS— $\dot{\delta}$
100	float	mas yr ⁻¹	Y	pmDE_error_TGAS	Standard error of proper motion in DE from TGAS
101	float	mas	Y	parallax_TGAS	Parallax from TGAS
102	float	mas	Y	parallax_error_TGAS	Standard error of parallax from TGAS
103	float	mag	Y	phot_g_mean_mag_TGAS	G-band mean magnitude from TGAS
104	float	e-/s	Y	phot_g_mean_flux_TGAS	G-band mean flux from TGAS
105	float	e-/s	Y	phot_g_mean_flux_error_TGAS	Error on G-band mean flux from TGAS
106	char	-	Y	ID_Hipparcos	Hipparcos target designation
107	char	...	Y	ID_TYCHO2	Tycho-2 target designation
108	float	arcsec	Y	Dist_TYCHO2	Center distance to target catalog
109	char	...	Y	MatchFlag_TYCHO2	Crossmatch quality flag (Note 6)
110	float	mag	Y	BTmag_TYCHO2	B_T magnitude from Tycho-2
111	float	mag	Y	eBTmag_TYCHO2	Error on B_T mag from Tycho-2
112	float	mag	Y	VTmag_TYCHO2	V_T magnitude from Tycho-2
113	float	mag	Y	eVTmag_TYCHO2	Error V_T magnitude from Tycho-2
114	float	mas yr ⁻¹	Y	pmRA_TYCHO2	Proper motion RA from Tycho-2
115	float	mas yr ⁻¹	Y	epmRA_TYCHO2	Error proper motion RA from Tycho-2
116	float	mas yr ⁻¹	Y	pmDE_TYCHO2	Proper motion DE from Tycho-2
117	float	mas yr ⁻¹	Y	epmDE_TYCHO2	Error proper motion DE from Tycho-2
118	char	...	Y	ID_UCAC4	UCAC4 target designation
119	float	arcsec	Y	Dist_UCAC4	Center distance to target catalog
120	char	...	Y	MatchFlag_UCAC4	Crossmatch quality flag (Note 7)
121	float	mas yr ⁻¹	Y	pmRA_UCAC4	Proper motion RA from UCAC4
122	float	mas yr ⁻¹	Y	epmRA_UCAC4	Error proper motion RA from UCAC4
123	float	mas yr ⁻¹	Y	pmDE_UCAC4	Proper motion DE from UCAC4
124	float	mas yr ⁻¹	Y	epmDE_UCAC4	Error proper motion DE from UCAC4
125	char	...	Y	ID_PPMXL	PPMXL target designation
126	float	arcsec	Y	Dist_PPMXL	Center distance to target catalog

Table 7
(Continued)

Col.	Format	Units	NULL	Label	Explanations
127	char	...	Y	MatchFlag_PPMXL	Crossmatch quality flag (Note 7)
128	float	mas yr ⁻¹	Y	pmRA_PPMXL	Proper motion RA from PPMXL
129	float	mas yr ⁻¹	Y	epmRA_PPMXL	Error proper motion RA from PPMXL
130	float	mas yr ⁻¹	Y	pmDE_PPMXL	Proper motion DE from PPMXL
131	float	mas yr ⁻¹	Y	epmDE_PPMXL	Error proper motion DE from PPMXL
132	char	...	Y	ID_2MASS	2MASS target designation
133	float	arcsec	Y	Dist_2MASS	Center distance to target catalog
134	char	...	Y	MatchFlag_2MASS	Crossmatch quality flag (Note 7)
135	double	mag	Y	Jmag_2MASS	<i>J</i> magnitude
136	double	mag	Y	eJmag_2MASS	Error <i>J</i> magnitude
137	double	mag	Y	Hmag_2MASS	<i>H</i> magnitude
138	double	mag	Y	eHmag_2MASS	Error <i>H</i> magnitude
139	double	mag	Y	Kmag_2MASS	<i>K</i> magnitude
140	double	mag	Y	eKmag_2MASS	Error <i>K</i> magnitude
141	char	...	Y	ID_ALLWISE	<i>WISE</i> target designation
142	double	arcsec	Y	Dist_ALLWISE	Center distance to target catalog
143	char	...	Y	MatchFlag_ALLWISE	Crossmatch quality flag (Note 7)
144	double	mag	Y	W1mag_ALLWISE	<i>W1</i> magnitude
145	double	mag	Y	eW1mag_ALLWISE	Error <i>W1</i> magnitude
146	double	mag	Y	W2mag_ALLWISE	<i>W2</i> magnitude
147	double	mag	Y	eW2mag_ALLWISE	Error <i>W2</i> magnitude
148	double	mag	Y	W3mag_ALLWISE	<i>W3</i> magnitude
149	double	mag	Y	eW3mag_ALLWISE	Error <i>W3</i> magnitude
150	double	mag	Y	W4mag_ALLWISE	<i>W4</i> magnitude
151	double	mag	Y	eW4mag_ALLWISE	Error <i>W4</i> magnitude
152	char	...	Y	cc_flags_ALLWISE	Prioritized artifacts affecting the source in each band
153	int	...	Y	ext_flg_ALLWISE	Probability source morphology is not consistent with single PSF
154	char	...	Y	var_flg_ALLWISE	Probability that flux varied in any band greater than amount expected from unc.s
155	char	mag	Y	ph_qual_ALLWISE	Photometric quality of each band (A = highest, U = upper limit)
156	double	arcsec	Y	Dist_APASSDR9	Center distance to target catalog
157	char	...	Y	MatchFlag_APASSDR9	Crossmatch quality flag (Note 7)
158	double	mag	Y	Bmag_APASSDR9	<i>B</i> magnitude
159	double	mag	Y	eBmag_APASSDR9	Error <i>B</i> magnitude
160	double	mag	Y	Vmag_APASSDR9	<i>V</i> magnitude
161	double	mag	Y	eVmag_APASSDR9	Error <i>V</i> magnitude
162	double	mag	Y	gpmag_APASSDR9	<i>g'</i> magnitude
163	double	mag	Y	egpmag_APASSDR9	Error <i>g'</i> magnitude
164	double	mag	Y	rpmag_APASSDR9	<i>r'</i> magnitude
165	double	mag	Y	erpmag_APASSDR9	Error <i>r'</i> magnitude
166	double	mag	Y	ipmag_APASSDR9	<i>i'</i> magnitude
167	double	mag	Y	eipmag_APASSDR9	Error <i>i'</i> magnitude
168	char	...	Y	ID_DENIS	DENIS target designation
169	double	arcsec	Y	Dist_DENIS	Center distance to target catalog
170	char	...	Y	MatchFlag_DENIS	Crossmatch quality flag (Note 7)
171	double	mag	Y	Imag_DENIS	<i>I</i> magnitude
172	double	mag	Y	eImag_DENIS	Error <i>I</i> magnitude
173	double	mag	Y	Jmag_DENIS	<i>J</i> magnitude
174	double	mag	Y	eJmag_DENIS	Error <i>J</i> magnitude
175	double	mag	Y	Kmag_DENIS	<i>K</i> magnitude
176	double	mag	Y	eKmag_DENIS	Error <i>K</i> magnitude
177	char	...	Y	ID_USNOB1	USNOB1 target designation
178	double	arcsec	Y	Dist_USNOB1	Center distance to target catalog
179	char	...	Y	MatchFlag_USNOB1	Crossmatch quality flag (Note 7)
180	double	mag	Y	B1mag_USNOB1	<i>B1</i> magnitude
181	double	mag	Y	R1mag_USNOB1	<i>R1</i> magnitude
182	double	mag	Y	B2mag_USNOB1	<i>B2</i> magnitude
183	double	mag	Y	R2mag_USNOB1	<i>R2</i> magnitude
184	double	mag	Y	Imag_USNOB1	<i>I</i> magnitude
185	int	mas yr ⁻¹	Y	pmRA_USNOB1	Proper motion RA from USNOB1
186	int	mas yr ⁻¹	Y	epmRA_USNOB1	Error proper motion RA from USNOB1
187	int	mas yr ⁻¹	Y	pmDE_USNOB1	Proper motion DE from USNOB1
188	int	mas yr ⁻¹	Y	epmDE_USNOB1	Error proper motion DE from USNOB1
189	int	...	N	Obsdate	Observation date yyyyymmdd

Table 7
(Continued)

Col.	Format	Units	NULL	Label	Explanations
190	char	...	N	FieldName	Name of RAVE field (RA/DE)
191	int	...	N	FiberNumber	Number of optical fiber [1,150]
192	int	...	N	PlateNumber	Number of field plate [1..3]
193	double	day	N	MJD_OBS	Modified Julian date
194	char	...	N	LST_start	Exposure start in Local Sidereal Time
195	char	...	N	LST_end	Exposure end in Local Sidereal Time
196	char	-	N	UTC_start	Exposure start in Coordinated Universal Time
197	char	-	N	UTC_end	Exposure end in Coordinated Universal Time

Note. The contents of Table 7 can be accessed at doi.org/10.17876/rave/dr.5/001. (1) HEALPix values were computed using the resolution parameter $N_{\text{side}} = 4096$ (resolution index of 12) and the NESTED numbering scheme. Any lower-resolution index HEALPix value can be computed from the given one by dividing it by $4(12 - n)$, where $n < 12$ is the desired resolution index. (2) Originating from: *_K* indicates values from stellar parameter pipeline, *_N_K* indicates a calibrated value, *_c* indicates values from chemical pipeline, *_SPARV* indicates values of radial velocity pipeline (used in DR3 also). (3) Flag value of the form FGSH, F being for the entire plate, G for the 50 fibers group to which the fiber belongs. S flags the zero-point correction used: C for cubic and S for a constant shift. If H is set to * the fiber is close to a 15 fiber gap. For F and G the values can be A, B, C, D, or E; A = dispersion around correction lower than 1 km s^{-1} ; B = dispersion between 1 and 2 km s^{-1} ; C = dispersion between 2 and 3 km s^{-1} ; D = dispersion larger than 3 km s^{-1} ; E = less than 15 fibers available for the fit. (4) Flag of stellar parameter pipeline 0 = pipeline converged. 1 = no convergence. 2 = MATISSE oscillates between two values and the mean has been performed. 3 = results of MATISSE at the boundaries or outside the grid and the DEGAS value has been adopted. 4 = the metal-poor giants with $S/N < 20$ have been rerun by DEGAS with a scale factor (i.e., internal parameter of DEGAS) of 0.40. (5) Cross-identification flag as follows: *IRFM* Temperature derived from infrared flux method; *CTRL* Temperature computed via color- T_{eff} relations; *NO* No temperature derivation possible. (6) Morphological Flag n.th minimum distance to base spectrum given by one of the types *a, b, c, d, e, g, h, n, o, p, t, u, w* (see Matijević et al. 2012). (7) Cross-identification flag as follows: *A* = one association within 2 arcsec, *B* = two associations within 2 arcsec, *C* = more than two associations within 2 arcsec, *D* = nearest neighbor more than 2 arcsec away, *X* = no association found (within 10 arcsec limit).

obtained from spectra with a resolution of 7500 covering the CaT regime. This catalog can be accessed via doi.org/10.17876/rave/dr.5/001 and CDS/VizieR. The typical S/N of a RAVE star is 40 and the typical uncertainty in radial velocity is $< 2 \text{ km s}^{-1}$. Stellar parameters are derived from the DR4 stellar parameter pipeline, based on the algorithms of MATISSE and DEGAS, but an updated calibration improves the accuracy of the DR5 stellar parameters by up to 15%. This pipeline is valid for stars with temperatures between 4000 K and 8000 K. The uncertainties in T_{eff} , $\log g$, and $[M/H]$ are approximately 250 K, 0.4 dex, and 0.2 dex, respectively, but vary with stellar population and S/N. The best stellar parameters have $\text{Algo_Conv} = 0$, $S/N > 40$, and $c1 = n$, $c2 = n$, and $c3 = n$. An error spectrum has been computed for each observed spectrum, and it is then used to assess the uncertainties in the radial velocities and stellar parameters.

Temperatures from the IRFM are derived for $> 95\%$ of all RAVE stars, and the asteroseismically calibrated $\log g$ is provided for a subsample of stars that can be calibrated asteroseismically ($\sim 45\%$ of the RAVE sample). The RAVE stars in the asteroseismically calibrated sample are given in doi.org/10.17876/rave/dr.5/002 and described in Table 8 of Appendix B. As in Matijević et al. (2012), binarity and morphological flags are given for each spectrum. Photometric information and proper motions are compiled for each star.

The abundances of Al, Si, Ti, Fe, Mg, and Ni are provided for approximately two-thirds of the RAVE stars. These are generally good to ~ 0.2 dex, but their accuracy varies with S/N, and for some elements also with the stellar population. Distances, ages, masses, and the interstellar extinctions are computed using the methods presented in Binney et al. (2014), but upgraded, especially for the more metal-poor stars.

The astrometry and parallaxes from the first *Gaia* data combined with the RAVE DR5 radial velocities ensure that uncertainties of 10 km s^{-1} in space velocities for 70% of the RAVE-TGAS stars can be derived. Further, because *Gaia*

astrometry provides completely new constraints on distances and tangential velocities, we can now use the RAVE pipelines to derive yet more accurate stellar parameters and distances for the TGAS stars, and even improve the parameters and distances of RAVE stars that are not in TGAS. The RAVE stars that have TGAS counterparts are provided in doi.org/10.17876/rave/dr.5/004.

Funding for RAVE has been provided by: the Australian Astronomical Observatory; the Leibniz-Institut fuer Astrophysik Potsdam (AIP); the Australian National University; the Australian Research Council; the French National Research Agency; the German Research Foundation (SPP 1177 and SFB 881); the European Research Council (ERC-StG 240271 Galactica); the Istituto Nazionale di Astrofisica at Padova; The Johns Hopkins University; the National Science Foundation of the USA (AST-0908326); the W. M. Keck foundation; the Macquarie University; the Netherlands Research School for Astronomy; the Natural Sciences and Engineering Research Council of Canada; the Slovenian Research Agency; the Swiss National Science Foundation; the Science & Technology Facilities Council of the UK; Opticon; Strasbourg Observatory; and the Universities of Groningen, Heidelberg, and Sydney. Based on data products from observations made with ESO Telescopes at the La Silla Paranal Observatory under programme ID 188.B-3002.

APPENDIX A APPENDIX BOOKKEEPING

In total, there are 2505 RAVE DR4 stars that are not in this data release. These fall into five categories:

1. Doubled field—identical field was published twice under a different name

20060123_0456m20 is doubled with 20060126_0456m20

Table 8
Description of the Asteroseismically Calibrated Red Giant Catalog

Col.	Format	Units	NULL	Label	Explanations
1	char(32)	...	N	RAVE_OBS_ID	Target designation
2	float	dex	Y	logg_SC	Log gravity calibrated asteroseismically (V16)
3	float	dex	Y	elogg_SC	Error on logg_MV (V16)
4	int	dex	Y	Flag050	Difference between logg_MV and logg_K is less than 0.5 dex. 1 = true 0 = false
5	int	dex	Y	Flag075	Difference between logg_MV and logg_K is less than 0.75 dex. 1 = true 0 = false
6	int	dex	Y	Flag_M	Normal star, meaning c1–c20 are all “n”. 1 = true 0 = false
7	float	K	Y	Teff_IR	Temperature from infrared flux method
8	float	dex	Y	Mg	Abundance of Mg [Mg/H]
9	int	...	Y	Mg_N	Number of spectral lines used for calculation of abundance
10	float	dex	Y	Al	Abundance of Al [Al/H]
11	int	...	Y	Al_N	Number of spectral lines used for calculation of abundance
12	float	dex	Y	Si	Abundance of Si [Si/H]
13	int	...	Y	Si_N	Number of spectral lines used for calculation of abundance
14	float	dex	Y	Ti	Abundance of Ti [Ti/H]
15	int	...	Y	Ti_N	Number of spectral lines used for calculation of abundance
16	float	dex	Y	Fe	Abundance of Fe [Fe/H]
17	int	...	Y	Fe_N	Number of spectral lines used for calculation of abundance
18	float	dex	Y	Ni	Abundance of Ni [Ni/H]
19	int	...	Y	Ni_N	Number of spectral lines used for calculation of abundance
20	float	dex	Y	Alpha_c	Alpha-enhancement from chemical pipeline
21	float	...	Y	CHISQ_c	χ^2 of the chemical pipeline
22	float	...	Y	frac_c	Fraction of spectrum used for calculation of abundances
23	float	mag	Y	AV_Schlegel	Total extinction in V-band from Schlegel et al. (1998)
24	float	kpc	Y	distance	Spectrophotometric distance (Binney et al. 2014)
25	float	kpc	Y	e_distance	Error on distance (Binney et al. 2014)
26	float	mag	Y	log_Av	Log Av extinction (Binney et al. 2014)
27	float	mag	Y	elog_Av	Error on log_Av (Binney et al. 2014)
28	float	mas	Y	parallax	Spectrophotometric parallax (Binney et al. 2014)
29	float	mas	Y	e_parallax	Error on parallax (Binney et al. 2014)
30	float	mag	Y	DistanceModulus_Binney	Distance modulus (Binney et al. 2014)
31	float	mag	Y	eDistanceModulus_Binney	Distance modulus (Binney et al. 2014)
32	float	...	Y	Fit_QUALITY_Binney	Given by symbol “F” in Equation (15) of Binney et al. (2014)
33	float	...	Y	FitFLAG_Binney	See final paragraph Section 3 of Binney et al. (2014)
34	float	...	Y	N_Gauss_fit	Number of components required for multi-Gaussian distance modulus fit
35	int	...	Y	Gauss_mean_1	Property of multi-Gaussian distance modulus fit, see Section 9, Equation (5)
36	float	...	Y	Gauss_sigma_1	Property of multi-Gaussian distance modulus fit, see Section 9, Equation (5)
37	float	...	Y	Gauss_frac_1	Property of multi-Gaussian distance modulus fit, see Section 9, Equation (5)
38	float	...	Y	Gauss_mean_2	Property of multi-Gaussian distance modulus fit, see Section 9, Equation (5)
39	float	...	Y	Gauss_sigma_2	Property of multi-Gaussian distance modulus fit, see Section 9, Equation (5)
40	float	...	Y	Gauss_frac_2	Property of multi-Gaussian distance modulus fit, see Section 9, Equation (5)
41	float	...	Y	Gauss_mean_3	Property of multi-Gaussian distance modulus fit, see Section 9, Equation (5)
42	float	...	Y	Gauss_sigma_3	Property of multi-Gaussian distance modulus fit, see Section 9, Equation (5)
43	float	...	Y	Gauss_frac_3	Property of multi-Gaussian distance modulus fit, see Section 9, Equation (5)

Note. The contents of Table 8 can be accessed at doi.org/10.17876/rave/dr.5/002.

20060123_0456m20 is removed

2. Renamed fields—fields that were renamed

20060627_0003m13 is renamed 20060629_0003m13

20070207_0734m34 is renamed 20070918_0734m34

3. Incorrect FITS headers—coordinates in header do not appear to be correct, so the proper stars that were observed cannot be identified; these fields were removed

20050814_2314m31

20060629_0003m13

4. Poor quality fields that were released in DR4

20110705_2028m00b

20091201_0206m84

5. DR4 stars with $S/N < 10$, spectra of too poor quality to process

We are left with 296 DR4 stars with $S/N > 10$ that were not able to be processed with SPARV.

APPENDIX B APPENDIX MATERIAL

The descriptions of the individual columns of the main DR5 catalog are specified in Table 7, and the descriptions of the individual columns of the asteroseismically calibrated red giant

catalog are specified in Table 8. The catalogs are accessible online at <http://www.rave-survey.org> and via the CDS VizieR service.

REFERENCES

- Adibekyan, V., Figueira, P., Santos, N., et al. 2013, *A&A*, 554, 44
- Alonso, A., Arribas, S., & Martínez-Roger, C. 1996, *A&AS*, 117, 227
- Alvarez, R., & Plez, B. 1998, *A&A*, 330, 1109
- Anguiano, B., De Silva, G. M., Freeman, K., et al. 2016, *MNRAS*, 457, 2078
- Anguiano, B., Zucker, D. B., Scholz, R.-D., et al. 2015, *MNRAS*, 451, 1229
- Antoja, T., Monari, G., Helmi, A., et al. 2015, *ApJ*, 800, 32
- Arce, H. G., & Goodman, A. A. 1999, *ApJL*, 512, L135
- Astratmadja, T. L., & Bailer-Jones, C. A. L. 2016, *ApJ*, 833, 119
- Bailer-Jones, C. A. L. 2015, *PASP*, 127, 994
- Bedding, T. R., Mosser, B., Huber, D., et al. 2011, *Natur*, 471, 608
- Bensby, T., Feltzing, S., & Oey, M. S. 2014, *A&A*, 562, A71
- Bienaymé, O., Famaey, B., Siebert, A., et al. 2014, *A&A*, 571, 92
- Bijaoui, A., Recio-Blanco, A., de Laverny, P., & Ordenovic, C. 2012, *StMet*, 9, 55
- Binney, J., Burnett, B., Kordopatis, G., et al. 2014, *MNRAS*, 437, 351
- Blackwell, D. E., & Shallis, M. J. 1977, *MNRAS*, 180, 177
- Blackwell, D. E., Shallis, M. J., & Selby, M. J. 1979, *MNRAS*, 188, 847
- Blanco-Cuaresma, S., Soubiran, C., Jofré, P., & Heiter, U. 2014, *A&A*, 566, 98
- Boeche, C., Chiappini, C., Minchev, I., et al. 2013, *A&A*, 553, 19
- Boeche, C., Siebert, A., Piffl, T., et al. 2014, *A&A*, 568, A71
- Boeche, C., Siebert, A., Williams, M., et al. 2011, *AJ*, 142, 193
- Bovy, J. 2015, *AJ*, 216, 29
- Bragaglia, A., Sestito, P., Villanova, S., et al. 2008, *A&A*, 480, 79
- Breddels, M. A., Smith, M. C., Helmi, A., et al. 2010, *A&A*, 511, A90
- Bressan, A. A., Marigo, P., Girardi, L., et al. 2012, *MNRAS*, 427, 127
- Burnett, B., & Binney, J. 2010, *MNRAS*, 407, 339
- Carrera, R., Pancino, E., Gallart, C., & del Pino, A. 2013, *MNRAS*, 434, 1681
- Carretta, E., Bragaglia, A., Gratton, R., & Lucatello, S. 2009, *A&A*, 505, 139
- Carretta, E., Bragaglia, A., Gratton, R. G., & Tosi, M. 2014, *A&A*, 422, 951
- Casagrande, L., Portinari, L., & Flynn, C. 2006, *MNRAS*, 373, 13
- Casagrande, L., Portinari, L., Glass, I. S., et al. 2014, *MNRAS*, 439, 2060
- Casagrande, L., Ramírez, I., Meléndez, J., Bessell, M., & Asplund, M. 2010, *A&A*, 512, A54
- Casagrande, L., Silva Aguirre, V., Schlesinger, K. J., et al. 2016, *MNRAS*, 455, 987
- Casagrande, L., Silva Aguirre, V., Stello, D., et al. 2014, *ApJ*, 787, 110
- Casey, A. R., Hawkins, K., Hogg, D. W., et al. 2016, arXiv:1609.02914
- Cayrel, R., Depagne, E., Spite, M., et al. 2004, *A&A*, 416, 1117
- Cordero, M. J., Pilachowski, C. A., Johnson, C. I., et al. 2014, *ApJ*, 780, 94
- Davies, G. R., & Miglio, A. 2016, *AN*, 337, 774
- De Silva, G. M., Freeman, K. C., Bland-Hawthorn, J., et al. 2015, *MNRAS*, 449, 2604
- Eisenstein, D. J., Weinberg, D. H., Agol, E., et al. 2011, *AJ*, 142, 72
- ESA 1997, The Hipparcos and Tycho Catalogues, ESA SP-1200
- Ford, A., Jeffries, R. D., & Smalley, B. 2005, *MNRAS*, 364, 272
- Fulbright, J. P., Wyse, R. F. G., Ruchti, G. R., et al. 2010, *ApJL*, 724, L104
- Funayama, H., Itoh, Y., Oasa, Y., et al. 2009, *PASJ*, 61, 931
- Gai, N., Basu, S., Chaplin, W. J., & Elsworth, Y. 2011, *ApJ*, 730, 63
- Gilmore, G., Randich, S., Asplund, M., et al. 2012, *Msngr*, 147, 25
- Górski, K. M., Hivon, E., Bandy, A. J., et al. 2005, *ApJ*, 622, 759
- Gratton, R. G., Sneden, C., Carretta, E., & Bragaglia, A. 2000, *A&A*, 354, 169
- Grevesse, N., & Sauval, A. J. 1998, *SSRv*, 85, 161
- Gustafsson, B., Edvardsson, B., Eriksson, K., et al. 2008, *A&A*, 486, 951
- Harris, W. E. 1996, *AJ*, 112, 1487
- Hawkins, K., Kordopatis, G., Gilmore, G., et al. 2015, *MNRAS*, 447, 2046
- Heiter, U., Jofré, P., Gustafsson, B., et al. 2015, *A&A*, 582, 49
- Høg, E., Fabricius, C., Makarov, V. V., et al. 2000, *A&A*, 355, L27
- Holtzman, J. A., Shetrone, M., Johnson, J. A., et al. 2015, *AJ*, 150, 148
- Ishigaki, M. N., Aoki, W., & Chiba, M. 2013, *ApJ*, 771, 67
- Jeffries, R. D., Jackson, R. J., Cottaar, M., et al. 2014, *A&A*, 563, 94
- Jofré, P., Heiter, U., Soubiran, C., et al. 2014, *A&A*, 564, 133
- Johnson, C. I., & Pilachowski, C. A. 2010, *ApJ*, 722, 1373
- Kharchenko, N. V., Piskunov, A. E., Schilbach, E., Röser, S., & Scholz, R.-D. 2013, *A&A*, 558, 53
- Koch, A., & McWilliam, A. 2008, *AJ*, 135, 1551
- Kordopatis, G., Binney, J., Gilmore, G., et al. 2015, *MNRAS*, 447, 3526
- Kordopatis, G., Gilmore, G., Steinmetz, M., et al. 2013a, *AJ*, 146, 134
- Kordopatis, G., Gilmore, G., Wyse, R. F. G., et al. 2013b, *MNRAS*, 436, 3231
- Kordopatis, G., Recio-Blanco, A., de Laverny, P., et al. 2011, *A&A*, 535, A106
- Kordopatis, G. R. C. 2014, in Proc. Annual Meeting of the French Society of Astronomy and Astrophysics, AVE: Results and Updates from Data Release 4, ed. J. Ballet et al., 431
- Kos, J., Zwitter, T., Wyse, R., et al. 2014, *Sci*, 345, 791
- Kunder, A., Bono, G., Piffl, T., et al. 2014, *A&A*, 572, 30
- Mamajek, E. E., Lawson, W. A., & Feigelson, E. D. 1999, *ApJ*, 516, 77
- Martell, S. L., Sharma, S., Buder, S., et al. 2017, *MNRAS*, 465, 3203
- Matijević, G., Zwitter, T., Bienaymé, O., et al. 2012, *ApJS*, 200, 14
- Michalik, D., Lindegren, L., & Hobbs, D. 2014, *A&A*, 574, A115
- Minchev, I., Chiappini, C., Martig, M., et al. 2014, *ApJL*, 781, L20
- Mishenina, T., Pignatari, M., Carraro, G., et al. 2015, *MNRAS*, 446, 3651
- Mosser, B., Belkacem, K., Goupil, M.-J., et al. 2010, *A&A*, 517, 22
- Munari, U. 1999, *BaltA*, 8, 73
- Munari, U., Henden, A., Frigo, A., et al. 2014, *AJ*, 148, 81
- Nidever, D. L., Zasowski, G., Majewski, S. R., et al. 2012, *ApJ*, 755, 25
- Nordström, B., Mayor, M., Andersen, J., et al. 2004, *A&A*, 418, 989
- Önehag, A., Gustafsson, B., & Korn, A. 2014, *A&A*, 562, 102
- Pancino, E., Carrera, R., Rossetti, A., et al. 2010, *A&A*, 511, 56
- Pasquini, L., Randich, S., Zoccali, M., et al. 2004, *A&A*, 424, 951
- Piffl, T., Binney, J., McMillan, P. J., et al. 2014a, *MNRAS*, 445, 3133
- Piffl, T., Scannapieco, C., Binney, J., et al. 2014b, *A&A*, 562, A91
- Ramírez, I., Allende Prieto, C., & Lambert, D. L. 2013, *ApJ*, 764, 78
- Reddy, B. E., Lambert, D. L., & Allende Prieto, C. 2006, *MNRAS*, 367, 1329
- Reddy, B. E., Tomkin, J., Lambert, D. L., & Allende Prieto, C. 2003, *MNRAS*, 340, 304
- Roederer, I. U., Preston, G. W., Thompson, I. B., et al. 2014, *AJ*, 147, 136
- Ruchti, G. R., Fulbright, J. P., Wyse, R. F. G., et al. 2011, *ApJ*, 737, 9
- Schlafly, E. F., & Finkbeiner, D. P. 2011, *ApJ*, 737, 103
- Schlaufman, K. C., & Casey, A. R. 2014, *ApJ*, 797, 13
- Schlegel, D. J., Finkbeiner, D. P., & Davis, M. 1998, *ApJ*, 500, 525
- Sharma, S., Bland-Hawthorn, J., Johnston, K. V., & Binney, J. 2011, *ApJ*, 730, 3
- Siebert, A., Williams, M. E. K., Siviero, A., et al. 2011, *AJ*, 141, 187
- Skrutskie, M. F., Cutri, R. M., Stiening, R., et al. 2006, *AJ*, 131, 1163
- Soubiran, C., & Girard, P. 2005, *A&A*, 438, 139
- Soubiran, C., Le Campion, J.-F., Cayrel de Strobel, G., et al. 2010, *A&A*, 515, 111
- Steinmetz, M., Zwitter, T., Siebert, A., et al. 2006, *AJ*, 132, 1645
- Stello, D., Bruntt, H., Preston, H., & Buzasi, D. 2008, *ApJ*, 674, 53
- Takeda, Y., Honda, S., Ohnishi, T., et al. 2013, *PASJ*, 65, 53
- Trevisan, M., Barbuy, B., Eriksson, K., et al. 2011, *A&A*, 535, 42
- Valenti, J. A., & Fischer, D. A. 2005, *ApJS*, 159, 141
- Valentini, M., Chiappini, C., & Davies, G. R. 2017, in press (arXiv:1609.03826)
- van Leeuwen, F. 2007, *A&A*, 474, 653
- Williams, M. E. K., Steinmetz, M., Binney, J., et al. 2013, *MNRAS*, 436, 101
- Wojno, J., Kordopatis, G., Steinmetz, M., et al. 2016a, *MNRAS*, 461, 4246
- Wojno, J., et al. 2016b, *MNRAS*, submitted (arXiv:1611.00733)
- Worley, C., de Laverny, P., Recio-Blanco, A., et al. 2012, *A&A*, 542, 48
- Xiang, M., Liu, X., Yuan, H., et al. 2014, *MNRAS*, 448, 822
- Yang, X. L., Chen, Y. Q., & Zhao, G. 2015, *AJ*, 150, 158
- Yanny, B., Rockosi, C., Newberg, H. J., et al. 2009, *AJ*, 137, 4377
- Zhao, G., Zhao, Y.-H., Chu, Y.-Q., Jing, Y.-P., & Deng, L.-C. 2012, *RAA*, 12, 723
- Zwitter, T., Matijević, G., Breddels, M. A., et al. 2010, *A&A*, 522, 54
- Zwitter, T., Siebert, A., Munari, U., et al. 2008, *AJ*, 136, 421